SEA ICE NEAR-INERTIAL RESPONSE TO ATMOSPHERIC STORMS

By

Chase Stoudt

RECOMMENDED:

Dr. William Hibler

Dr. Mark Johnson

Dr. Rolf Gradinger

Dr. Harper Simmons
Advisory Committee Chair

APPROVED:

Dr. Katrin Iken
Program Head, Marine Science and Limnology

Dr. Joan Braddock
Interim Dean, School of Fisheries and Ocean Sciences

Dr. John Eichelberger
Dean of the Graduate School

28 April 2015
Date

SEA ICE NEAR-INERTIAL RESPONSE TO ATMOSPHERIC STORMS

Presented to the Faculty
of the University of Alaska Fairbanks

in Partial Fulfillment of the Requirements
for the Degree of

MASTER OF SCIENCE

By
Chase A. Stoudt
B.S.

Fairbanks, Alaska

May 2015

Abstract

A moored oceanographic array was deployed on the Beaufort Sea continental slope from August 2008-August 2009 to measure Arctic sea ice near-inertial motion in response to rapidly changing wind stress. Upward looking Acoustic Doppler Current Profilers detected sea ice and measured ice drift using a combination of bottom track and error velocity. An analysis of in-situ mooring data in conjunction with data from National Center for Environmental Prediction (NCEP) reanalysis suggest that many high and low pressure systems cross the Beaufort in winter, but not all of these create a near-inertial ice response. Two unusually strong low pressure systems that passed near the array in December 2008 and February/March 2009 were accompanied by elevated levels of near-inertial kinetic energy in the ice. The analysis suggests pressure systems which have a diameter to ground track velocity ratio close to ¾ of the local inertial period can excite a large near-inertial response in the sea ice. It is conjectured that this results from the combined effect of resonance arising from similar intrinsic timescales of the storm and the local inertial period and from stresses that are able to overcome the damping of sea ice arising from ice-mechanics and damping in the ice-ocean boundary layer. Those systems whose intrinsic times scales do not approach resonance with the local inertial period did not excite a large near-inertial response in the sea ice. From an analysis of two storms in February 2009, and two in December 2008, it appears that wind stresses associated with previous low pressure systems preconditioned the ice pack, allowing for larger near-inertial response during subsequent events.

Table of Contents

Page

List of Figures

Page

List of Tables

1.0 Introduction

Sea ice plays an important role in regulating the Earth's climate. It acts to thermally insulate the Arctic atmosphere from the often warmer Arctic Ocean [*Cassano et al.*, 2013]. In addition, the advection of sea ice, its formation and melt, and transport in and out of the Polar regions, act as a climate moderator for the rest of the planet [*Koç et al.*, 2009].

The Arctic Ocean surface waters are atmospherically isolated during the winter, and open to the atmosphere in the summer with two strongly stratified layers in the upper 250 m. They consist of deeper waters separated from the upper layer by a strong halocline [*Carmack*, 2007]. Mixing of the Arctic Ocean is much weaker than the rest of the world's ocean basins and the low levels are attributed to the presence of sea ice, which acts to isolate the ocean from atmospheric disturbances [*Halle and Pinkel*, 2003]. One class of motions that may be an important moderator of energy transfer from the atmosphere and into the upper ocean is inertial oscillations [*Gill*, 1984]

1.1 Inertial oscillations

Wind blowing across sea ice transmits wind stress causing it to move. Neglecting any vertical or lateral stresses, sea ice is deflected by the Coriolis force after an initial wind impulse. It will then move in a circular orbit called an inertial oscillation. Consider a linear model of sea ice motion where friction and ice mechanics are neglected:

$$\frac{\partial u}{\partial t} = fv$$
$$\frac{\partial v}{\partial t} = -fu$$

where u and v are eastward and northward velocity, respectively, and $f = 2\Omega \cos\varphi$ where f is the Coriolis parameter and $\Omega = 7.2921 \times 10^{-5}$ rad/s is the rotation rate of the earth. The above equations are first order, linear differential equations that have the solution:

$$u = V \sin ft$$
$$v = V \cos ft$$

The solution has the form of a circular clockwise orbit for f>0, with a period $T = 2\pi f^{-1}$ and can describe inertial oscillations of the ocean or ice. For the latitude of the ICORTAS array the

inertial period is approximately 12.6 h. An example of inertial oscillations of an ocean drifter is shown below from Van Meurs [1998]. Ice in free drift will also loop inertially [*Heil and Hibler III.*, 2002].

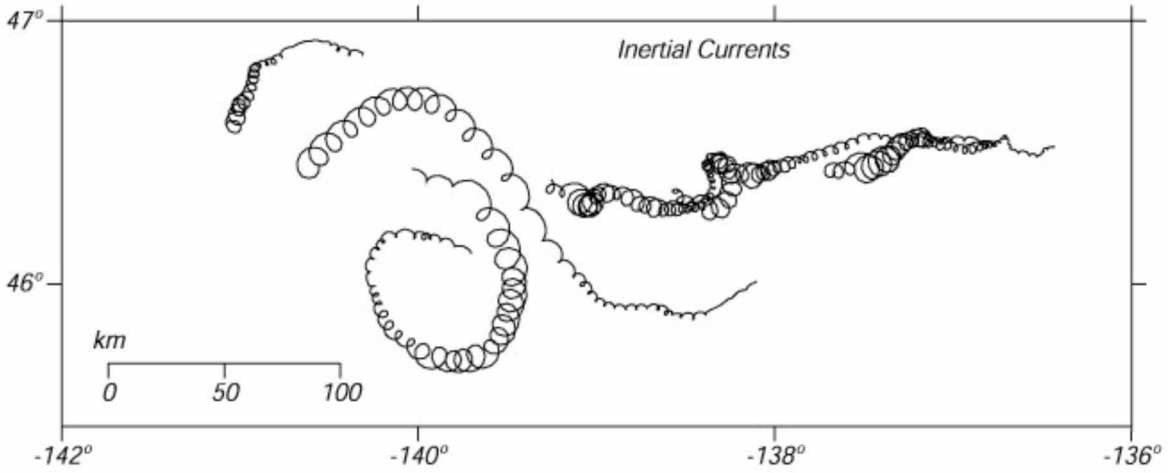

Figure 1: Inertial Oscillation example. Inertial currents in the North Pacific in October 1987 measured by holey-sock drifting buoys drogued at a depth of 15 meters. Inertial oscillations are evident in the tight looping, superimposed on drift arising from a background current. Figure from *Van Meurs* [1998].

I am motivated to study the ice near-inertial response because energy can leak into the stratified ocean below in the form of near-inertial internal gravity waves, via the "inertial pumping mechanism" [*Gill*, 1984]. This occurs when ice oscillatory motion causes divergence and convergence in the mixed layer that then pumps the pycnocline interface up and down, transferring energy from the atmosphere through sea ice into the ocean below. This exchange between the atmosphere and the ocean through the inertial pumping mechanism is an important link in the energy transfer cascade that links climate and other long-period, large-scale phenomena with small-scale effects, i.e., turbulence. Additionally shear-driven mixing at the base of the mixed layer can result in entrainment and deepening of the mixed layer [*Price et al.*, 1986].

As noted by Heil and Hibler III. [2002] and other authors, a more complete dynamical description can arise from a consideration of the ice-ocean boundary layer. Acknowledging the limitation of this, the scope of this thesis was limited to a consideration of in-situ measurements of ice-drift measured by upward looking Acoustic Doppler Current Profilers (ADCP). This thesis examines a high temporal resolution dataset over a fixed geographical area for an entire year, which has been difficult for other non-modeling studies.

1.2 Arctic Ocean bathymetry

The Arctic Ocean (Figure 2) is made up of three deep basins, with depths of over 4,300 m. On the Eurasian side, a broad continental shelf extends far into the interior Arctic Ocean, with the shallowest depths found in the Laptev, East Siberian and Chukchi seas. The continental shelves such as on the Siberian shelf [*Aagaard et al.*, 1981] are usually less than 200 m deep and extend as far as 600 km from shore. The Canadian Basin is separated from the Amundsen and Nansen basins by the Lomonosov Ridge, which extends 2000 km in a line from the north end of Greenland to Novosibirskiye. The mooring-based experiment of this study was situated on the continental slope of the Canadian Basin (Figures 2 and 3), and was influenced by

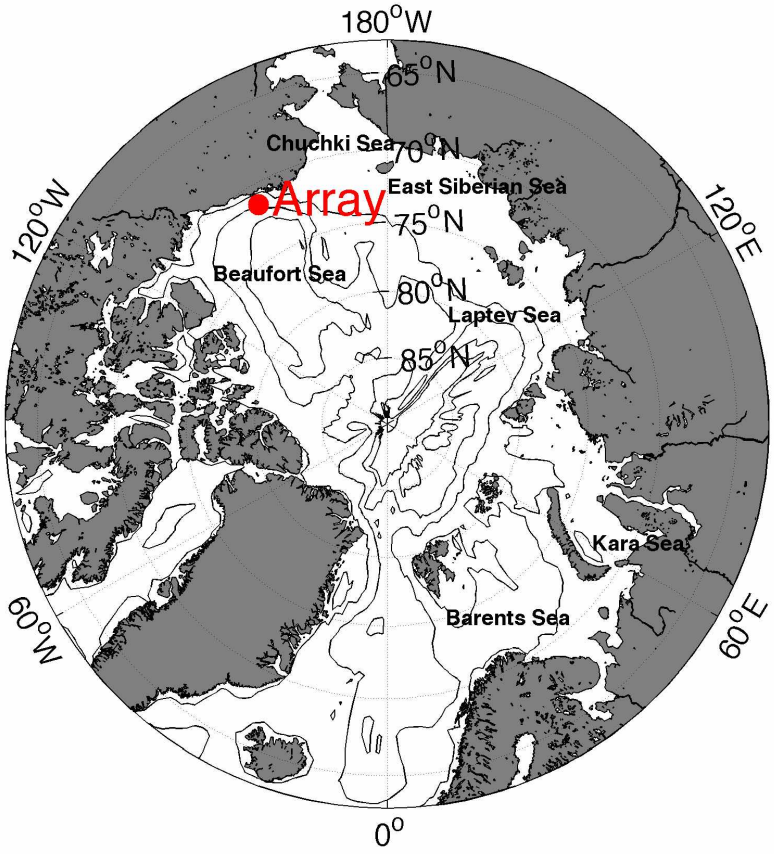

Figure 2: Map of Arctic Ocean with relevant seas labeled. The red dot indicates the location of the mooring array. A more detailed view of the mooring array is shown in Figure 3.

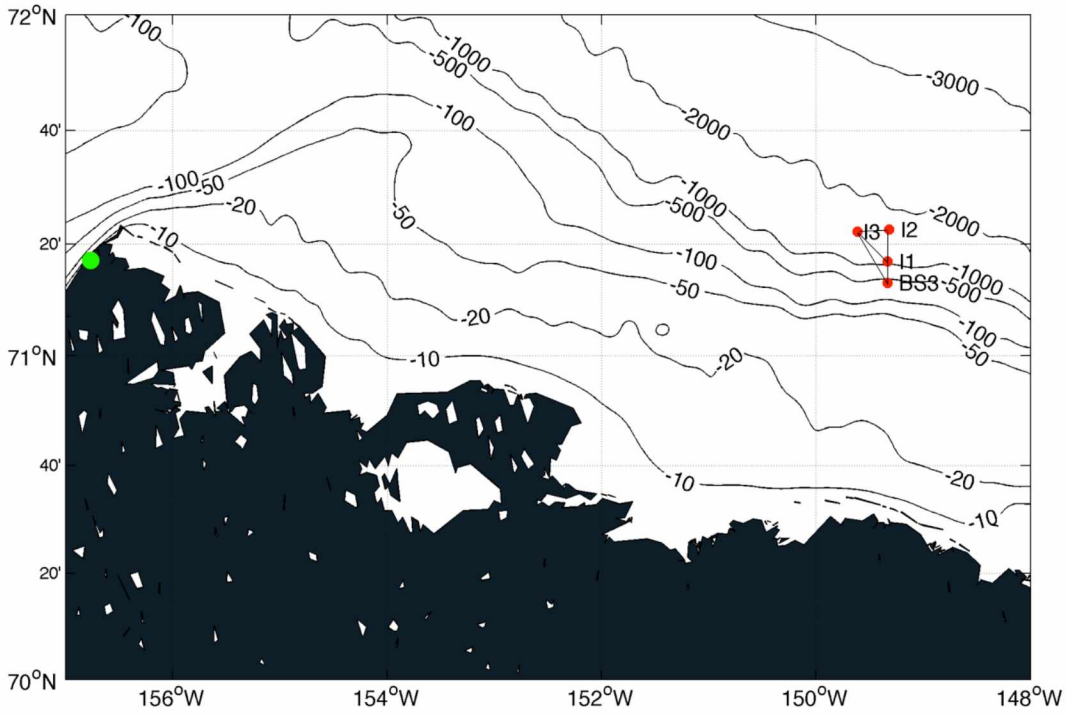

Figure 3: Map of the ICORTAS study area with depth contours labeled in meters. Moorings are marked as red dots. The Barrow Airport is marked with a green dot. The larger triangle indicates the 91.7 km^2 area covered by the mooring array that will later be compared to satellite ice-concentration measurements and the smaller triangle is the 54.7 km^2 area of the I1-I3 moorings used for divergence calculations.

both the interior Arctic and coastal ocean dynamics and the coupled dynamics of the atmosphere, ice and ocean. In addition, this area is part of the marginal ice zone.

1.3 Arctic sea ice and its effects on the ocean

The surface energy budget of the Arctic Ocean is dominated by the presence or absence of sea ice. Albedo is the ratio of the reflected to incoming shortwave solar radiation. Ice-free oceans typically have albedo of 0.10-0.15 and sea-ice albedo ranges from 0.8 to 0.98. Fresh snow cover can raise ice albedo to 0.98. Melt ponds during the spring result in albedo of 0.20-0.60. Since the albedo of ice is so high relative to the open ocean, sea ice considerably reduces the amount of solar radiation absorbed by the ocean below [*Perovich et al.*, 2007].

Another effect on the surface energy budget comes from the thermally insulating properties of sea ice. During the winter there is a large difference between the cold air and the relatively warm ocean below, and sensible heat flux is altered by sea ice. For example in winter, ice free conditions (i.e., in a polynya), fluxes are 50-100 W m^{-2} [*Fiedler et al.*, 2010] from ocean to atmosphere, whereas in winter, through sea ice fluxes are 10-15 W m^{-2} [*Kurtz et al.*, 2011]. During the summer ice free months, open ocean values range from 90-100 W m^{-2} from the atmosphere into the ocean [*Berry and Kent*, 2011]. The majority of winter heat transfer occurs primarily around the perimeter of the Arctic Ocean where leads, polynyas, and seasonal sea ice allow heat to move from the ocean to the atmosphere. Arctic cyclones (low pressure systems) and large scale wind forcing can cause sea ice to diverge, thus offering a direct path for kinetic energy transfer into the ocean interior. However, large, long-lasting openings in the ice are rare in winter (except in polynya formation areas); therefore, kinetic energy transfer from the atmosphere into the ocean is generally weak [*Lammert et al.*, 2009]. Vertical mixing and ocean-to-ice heat flux is quite low in the Arctic Ocean. This is the primary reason the interior Arctic Ocean remains ice covered year round [*Stranne and Bjork*, 2012]. Modeling studies of sea ice have shown that an increase in vertical heat flux in the Arctic would cause a reduction in ice cover, where sea ice distribution would resemble the seasonal Antarctic cover that disappears every year [*Cassano et al.*, 2013]. An increase in small diameter, fast moving Arctic cyclones accompanied by the opening of transient leads, could increase the heat transfer from the ocean to the atmosphere during the ice covered months along with an increase of kinetic energy in the upper ocean. Future climate change may also play a role by further reducing sea ice

concentrations, thereby increasing the possibility of transient leads in the ice covered season [*Pickart et al.*, 2009]. In a study of ice edge upwelling Lepparanta and Hibler III. [1985] found that, apart from differences in drag, in a steady state situation the sea ice margin could not induce upwelling. In addition, Lepparanta and Hibler III. [1985] suggest that fluctuating inertial variability may induce upwelling.

Sea ice formation also plays a large role in oceanic circulation. Brine rejection causes the density to increase in the underlying ocean. Sea ice transport out of the Arctic brings a substantial salt flux to the underlying waters while introducing a large freshwater flux into Greenland Sea [*Aagaard and Greisman*, 1975]. This phenomenon induces convection with magnitude depending on the salt content of the original seawater. Long-term wind stress can cause a sea surface height gradient that can dominate sea ice motion. This signal can mask high frequency events unless local wind reversals are strong [*Hibler III. and Bryan*, 1987].

The Arctic Ocean ice cover and the associated air sea surface boundary layer processes are very complicated. Throughout the entire year, a large difference in sea ice types exist due to seasonal cycles of sea ice growth and melt combined with sea ice transport and deformation [*Stroeve et al.*, 2012]. These ice types range from grease ice to rafted pack ice that may include first-year and multi-year ice. The ice pack itself floats on an ocean with variable currents that carry heat, salt and momentum. The opening and closing of transient floes cause the Arctic Ocean to have one of the most complex surface boundary conditions of any ocean in the world, and make sampling the ocean below logistically challenging and dangerous.

Due to non-linear ice mechanics the ice cover can fracture into linear kinematic features [*Heil and Hibler III.*, 2002; *Hibler III.*, 2004] that form a structured pattern of stress into the ocean. These patterns can cause localized upwelling and downwelling. Oscillatory pulling and pushing of ice from and away from the coast combined with pack ice motion can allow substantial changes in the effective stress transmitted into the ocean. Hence, it is possible in some circumstances for significant wind energy to be transmitted into the ocean even with a thick ice pack.

1.4 Sea ice concentration in the Arctic

Sea ice concentration is defined as the ratio of area covered by ice to the total area at a given location. It is a function of size of the area under consideration. Following the standards put forth by the National Snow and Ice Data Center (NSIDC), any observed data cell containing

above 15% ice concentration qualifies as ice covered. Ice concentration is the major modulator of mechanical energy transfer between the atmosphere and the ocean, in part because mechanical energy transfer is related to wind stress on the surface of the ocean. In particular, sea ice stress at higher concentration reduces wind stress to the ocean [*Hibler III. and Bryan*, 1987]. A well-known rule of thumb is that pack ice moves with about 2% of the speed of the surface wind and about to 30° to the right of the wind [*Thorndike and Colony*, 1982]. Lower concentrations of sea ice allow for greater control of the ice movement by the underlying oceanic circulation, which can account for up to 50% of the ice motion [*Thorndike and Colony*, 1982]. In the past three decades, Arctic sea ice has experienced a dramatic decline in its extent and concentration [*Stranne and Bjork*, 2012]. This played a major role in the lowest ever observed sea ice extent in 2012, where preconditioning from decades of sea ice decline made the ice pack vulnerable to a strong storm that entered the Arctic in August 2012. The storm caused a massive separation of the consolidated ice pack and individual floes, allowing large amounts of atmospheric energy to easily transfer into the ocean below [*Parkinson and Comiso*, 2013].

1.5 Sea ice motion in the Beaufort

Large-scale sea ice motion in the Beaufort Sea is dominated by the Beaufort Gyre [*Asplin et al.*, 2009]. This gyre is driven by basin-scale geostrophic winds. These winds typically follow an anticyclonic (clockwise in the northern hemisphere) pattern, as does sea ice motion over this region. An anticyclonic wind pattern will lead to higher ice concentrations due to Ekman convergence. During summer months, the Beaufort Gyre can occasionally reverse to a cyclonic regime [*Proshutinsky and Johnson*, 1997] where lower sea level pressure is observed throughout the Arctic basin and many low-pressure systems are observed in the Southern Beaufort Ocean [*Pickart et al.*, 2009].

Sea ice motion and concentration both depend on sea ice extent, gyre rotation and deformation within the gyre itself. A distinct yearly cycle is seen where sea ice deformation is highest in the fall and lowest mid-winter. Deformation and ice growth are highest on the edges of the gyre, which then promote 25-45% more seasonal sea ice growth [*Kwok*, 2006]. When the Beaufort Gyre is anticyclonic (clockwise) sea ice transport is away from the Canadian Archipelago and westward into the Chukchi Sea. During gyre reversals, this switches directions and sea ice transport is to the north from the Chukchi and Southern Beaufort and into the transpolar drift where it is exported through Fram Strait [*Proshutinsky and Johnson*, 1997].

1.6 Arctic storm characteristics

Arctic cyclones play an important role in the ice dynamics of the Arctic. Persistent storms can cause low ice conditions in one part of the Arctic while simultaneously increasing ice concentration in other parts. Storms can cause mesoscale sea ice convergence on the leading edge of the system and corresponding divergence and fractured ice on the trailing side [*Jacobs and Comiso*, 1989]. This phenomenon may swap depending on the direction of storm travel and location of the coastline (if any), but will always be balanced by the corresponding divergence/convergence on the opposite side of the system. From a thermodynamic standpoint, lower ice concentration can lead to increased heat and moisture transport from the ocean into the atmosphere when the ocean is warmer than the air. This would be most common in the autumn and early winter when first year sea ice is still forming and there is a large temperature gradient between the atmosphere and the ocean [*Cassano et al.*, 2013]. In addition, ice will generally be thinner and weaker during the autumn months in the beginning of the ice growth season [*Parkinson and Comiso*, 2013].

Central Arctic storms peak during the summer months. However, this signal is not as strong near the continental margins [*Serreze and Barret*, 2007]. Over the past 50 years there has been an increase in the intensity and frequency of Arctic storms throughout a whole year [*Asplin et al.*, 2009]. This has been linked to a shift in the Arctic Oscillation [*Serreze and Barret*, 2007], where sea level pressure anomalies have changed from positive in the Arctic basin and negative at mid-latitudes to negative in the Arctic basin and positive in the mid-latitudes.

1.7 Observational studies of near-inertial motion in sea ice

Observations of near-inertial oscillations have been made in oceans and lakes around the world for many years [*Pollard and Millard*, 1970]. During the Arctic Ice Dynamics Joint Experiment (AIDJEX), several inertial loops were observed superimposed over a mean flow with each cycle having a period of approximately 12 h during one event in August, which lasted 3 days [*Khandekar*, 1980]. The data were collected at the drilling site Kopanoar, located roughly at 70°23'N and 135°06'W. This site was located in the Canadian Archipelago on the southern side of Banks Island and was bounded by coastline to the north and south. This differs from the Ice Covered Oceanic Response to Atmospheric Storms (ICORTAS) array, which was bounded to the south and has no immediate northern shoreline. Khandekar [1980] suggested that the observed ice motion was associated with temporal variation of surface wind stress, and

sinusoidal variations in ice velocities were observed with periods ranging from a minimum of 10 h to a maximum of 15 h. The inertial period at this latitude is a little over 12 h, similar to the inertial period at the ICORTAS array. In the AIDJEX study, ice floe inertial motion velocities ranged from 20 to 80 cm s^{-1}. Oscillatory wind stress in both time and direction was also observed, followed by a steady wind direction. Sea ice movement no longer exhibited inertial behavior after the winds were steady. More recently [*Lammert et al.*, 2009] observed a cyclone pass over an array of air launched ice drift buoys in the FRAMZY (Fram Strait cyclones; in German: Framstraßen-Zyklonen) experiment. They found that near-inertial sea ice oscillations were observed when the advective timescale of the storm was close to the inertial period. They defined the advective timescale of the storm as $T_S = D/U$, where D is the storm diameter and U is the storm ground track speed. The optimal conditions for a strong inertial response were found when $T_S \sim 3/4\ T_I$, where T_I is the inertial period. In addition, they observed a small amount of divergence; however, they noted no such statistics of near-inertial sea ice oscillations were available due to inadequate temporal sampling. The ICORTAS array was unique because it was spatially fixed and not moving with the ice.

Detailed deformation measurements on a temporal and spatial scale similar to the ICORTAS array [*Hibler III. et al.*, 1974] revealed strong inertial deformation at the inertial frequency, which tended to occur in conditions where the pack ice had relaxed slightly and was not highly stressed. Most subsequent buoy data taken were not accurate enough and not sampled frequently enough to resolve inertial variability. Exceptions to this were German buoy data analyzed by [*Heil and Hibler III.*, 2002] in a somewhat more tidally active region (the Eurasian basin), which was found to have strong inertial variability, and was generally explained by inertial variability without tidal forcing. More detailed buoy data taken by Hutchings et al. [2005] resolved the inertial peak and showed a strong deformation signal that was greatly damped by ice mechanics in winter. This agrees with the original Heil and Hibler III. [2002] results taken in the spring, where analysis of the time series showed periods when no inertial signal was present when the ice pack was under compressive stress with low deformation. Hutchings et al. [2005] showed an inertial signal in winter, but observed a summer signal several orders of magnitude higher. Simulations with an ice ocean tidal model reproduced this with the additional conclusion that tidal forcing alone reproduces effectively none of this behavior, and certainly not the magnitude variation [*Heil et al.*, 2008; *Hibler III. et al.*, 1983].

1.8 Tides and near-inertial motion

The M2 tide has a period of 12.42 h and the local inertial period is 12.6 h. Hence, tidal- and wind-generated oscillations have very close frequencies at the latitude of the ICORTAS ADCP array. The different types of oscillations can sometimes be distinguished by direction in which current vectors rotate. Tides can cause circular orbits in both clockwise and counterclockwise directions; however, wind-generated inertial oscillations will only rotate in the clockwise direction in the northern hemisphere. Arctic tidal models [*Kowalik and Proshutinsky*, 1993; *Padman and Erofeeva*, 2004] suggest semidiurnal velocities of no more than 2 cm s^{-1} in this region, whereas the greatest transient ADCP observed signals are 20 cm s^{-1}. The dominant sense of rotation in this region is anticyclonic but may change depending on the climatic regime [*Proshutinsky et al.*, 2002]. Martini et al. [2014] found an increase of 0.2 m s^{-1} in the ocean near-inertial signal during the same events this thesis examines, suggesting that the observed velocity episodic increase in inertial currents was associated with a wind-driven event. Tidal forcing in conjunction with Arctic storms can also cause inertial/tidal motion and deformation [*Heil and Hibler III.*, 2002; *Hibler III. et al.*, 1974; *Hibler III. et al.*, 2006] with concentrated motion along linear kinematic features [*Hutchings et al.*, 2005]. These ice mechanics induced features can transmit considerable surface stress into the ocean surface even in the presence of thick ice. Tidal motion is also a persistent phenomenon, whereas inertial motion is episodic. This difference helps distinguish between the two.

1.9 The Ice Covered Oceanic Response to Atmospheric Storms (ICORTAS) project

The ICORTAS project was a mooring-based experiment to study the spin-up and spin-down of inertial energy in an ice covered ocean. Sea ice was detected and tracked by upward looking ADCP deployed for one year beginning in the summer of 2008 in the Beaufort Sea. The moorings were spaced approximately 10.5 km apart and each mooring had and upward looking ADCP at 80 m below the surface. The array was located 150 km east of Barrow, Alaska (Figure 3).

Using the ICORTAS measurements of ocean currents, temperature and salinity, Martini et al. [2014] showed downward propagating near-inertial internal waves during the middle of winter. In contrast with the oceanographic focus of Martini et al. [2014], this thesis uses ICORTAS data to focus on the near-inertial motions of the sea ice itself. Specific questions that are addressed are:

1) What additional value was obtained from four individual ADCP derived estimates of sea ice concentration in an 40 m^2 ADCP footprint versus a multi-mooring ensemble estimate of sea ice concentration with a nominal coverage area of 91.7 km^2 (larger triangle in Figure 3) vs. that obtained from the nearest 625 km^2 SSMI grid pixel. What do we learn from the ADCP estimates that do not have the spatial and temporal biases of SSMI?
2) Can we identify sea ice inertial motions in response to the wind?
3) How often do wind forced sea ice near-inertial oscillations occur and what system characteristics cause these oscillations in the Beaufort?

Given the location of the ICORTAS array on the Beaufort Slope just beyond the shelf break, ice concentrations may be affected by along-shore and cross-shore winds as well as tidal and inertial variations in sea ice drift. Near-inertial oscillations are common; however, very few year-long high temporal resolution Eulerian studies have been done in the Arctic [*Heil and Hibler III.*, 2002]. I was fortunate to observe seven storm events: five large events that had storm timescales forcing parameters at or close to the resonant frequency and two events that produced a less energetic response due to the wrong time and space scales. However, while no long temporal studies have been done, shorter temporal studies of deformation in the Beaufort sea [*Hibler III. et al.*, 1974] and deformation and drift [*Kwok et al.*, 2003] in the Central Arctic have shown that deformation and drift at the near inertial period are the rule not the exception.

2.0 Methods

In addition to the mooring data, several additional data sources were used for this study. Satellite microwave derived sea ice concentrations from the Special Sensor Microwave Imager (SSMI) were used to compare and contrast the derived concentration data from the moorings. SSMI level 3 data products [*Nolin et al.*, 1998] were obtained for the ICORTAS mooring deployment time period. SSMI is a passive microwave space-based sensor on a polar orbiting satellite that provides daily ice percentage data over the entire Arctic with a resolution of 25 x 25 km. SSMI bootstrapped ice percentage values were examined from the National Climate Data Center for the time period of the mooring deployment.

Advanced Microwave Scanning Radiometer (AMSRE) data from NSIDC were considered and rejected, as data acquired from this remote sensing platform were insufficient in temporal and geographical resolution to distinguish individual events due to cloud cover and orbital parameters. Advanced High Resolution Radiometer (AVHRR) brightness temperature

data were used to aide in the interpretation of both the SSMI and ADCP ice concentrations [*Fetterer and Hawkins*, 2003]. Data were accessed through the UAF Geographic Information Network of Alaska (GINA) swath viewer and covered approximately the same area as SSMI with a resolution 1 x 1 km. In-situ wind data were not available near the array. Surface wind speed and direction from the Barrow Post Will Rogers Airport were available (see Figure 3). This site was approximately 150 km southwest of the study site and the measurements were made 10 m above the ground. The National Center for Environmental Prediction (NCEP) weather reanalysis data in the form of wind velocities and atmospheric sea level pressures were utilized for storm characterization [*Kanamitsu et al.*, 2002].

Each mooring contained one upward looking, broadband Teledyne Workhorse 300 kHz (WHS300) ADCP deployed at a nominal 80 m depth. In the I1-I3 moorings, ice velocity was derived from acoustical bottom tracking, which gives the velocity of the reflective surface that is currently above the instrument. Each ensemble contained 8 pings and one ping transmitted every 40 sec (ensemble length was 5 min 20 sec), with a 2 min 40 sec wait time for a total of 8 min temporal resolution. This surface could be sea ice or open water, and distinguishing between the two was the first step in tracking sea ice. By comparing the properties of open water versus sea ice motion, a criterion can be defined that allows us to track sea ice motion. Mooring BS3 used a different tracking mode, Lowered Acoustic Doppler Current Profiler (LADCP), instead of bottom track. BS3 had 33 pings per ensemble, one ping every 7.3 sec (ensemble length was 4 min) and a 10-meter bin size, with a wait time of 56 min for a temporal resolution of 1 h.

2.1 Ice detection using the error velocity method

I used the error velocity [*Teledyne*, 2006] for detecting sea ice using the method of Visbeck and Fischer [1995]. The WHS300 has three acoustic beams that are used to calculate horizontal velocities. In addition, data from the fourth beam can be used to test the assumption of horizontal homogeneity. The Teledyne three-dimensional velocity calculations assume that the beams are all seeing the same flow field. Error velocity quantifies how well this assumption is being met by comparing the mismatch between all four beams. This mismatch is illustrated in Figure 4.

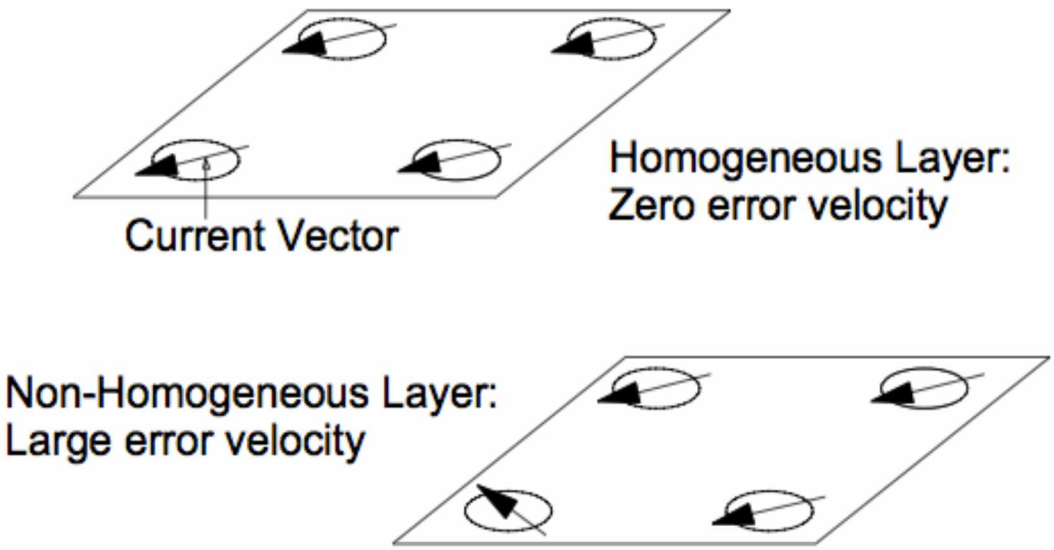

Figure 4: An illustration of horizontal homogeneity versus non-homogeneity (from Teledyne [2006]).

During periods of open water, the surface moves vertically with waves. Therefore, the assumption of horizontal homogeneity is violated and correspondingly, error velocity is high. When sea ice covers the ocean, the surface no longer moves vertically and effectively moves as a coherent horizontal unit instead. This is reflected as low error velocity.

A modified Visbeck and Fischer [1995] method was used on bottom track error velocity. In order to compare the hourly data from B3 with the eight minute data from the "I" moorings, ADCP bottom track and error velocity records were assembled to the same time base with a temporal resolution of 2 hours. Two measurements compose the B3 mean and 15 compose the "I" mooring ensembles. The bottom track error velocity signal was highpassed using a Hanning filter with window size of 3 days versus 6 hours in Visbeck and Fischer [1995] . This was chosen because the noise in a 6 hour window obscured the signal of sea ice versus open water, whereas 3 days was the optimum to distinguish between the two in this dataset. This bottom track error velocity time series data for all moorings are shown in Figure 5. By picking an empirical cutoff value of error velocity, ice presence can be detected. Figure 6 shows a histogram of error velocity for moorings B3, I1, I2 and I3. Moorings I1, I2, I3 showed more variation in sampling velocity than B3 because they were programmed with less pings per ensemble. Ice presence was indicated by the peak in low error velocity associated with large amounts of correlated horizontal motion. Since the site was ice covered for the majority of the year, any values that fall near the peak indicate times when the mooring was ice covered. Larger error velocity values to the right of the peak indicate open water. The base of this peak was chosen as the cutoff for no sea ice (0.015, 0.029, 0.032 and 0.03 mm s^{-1} for moorings B3, I1, I2 and I3 respectively) following [*Visbeck and Fischer*, 1995]. The data to the left of these values describe 90% of the error velocity variance, which was assumed to be sea ice. If a specific value of error velocity was higher than these values, that point was tagged as open water. If a specific error velocity fell below the cutoff, it was tagged as sea ice. The binary series resulting from this was used to color Figure 5 where red is ice covered and blue is open water. Erroneous data were removed by hand and corrections from ADCP tilt due to mooring blowdown were applied. Periods of calm winds (i.e., low surface error velocity) that could masquerade as ice covered data were identified and removed manually.

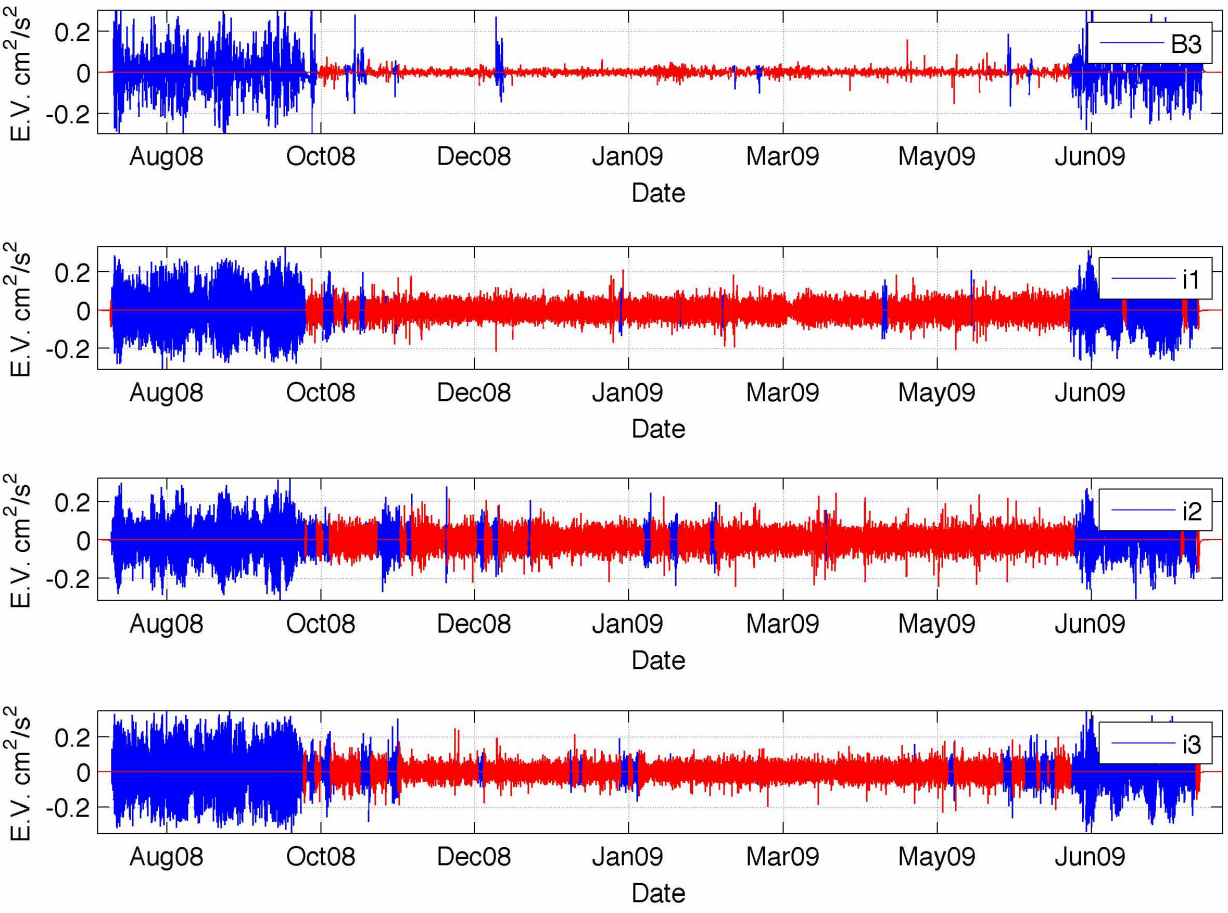

Figure 5: Bottom track error velocity time series. Blue colors indicate ice-free dates while red colors indicate ice covering the mooring array. Ice-free and ice-covered times are identified using the method of Section 2.1 and the histogram for each mooring in Figure 6.

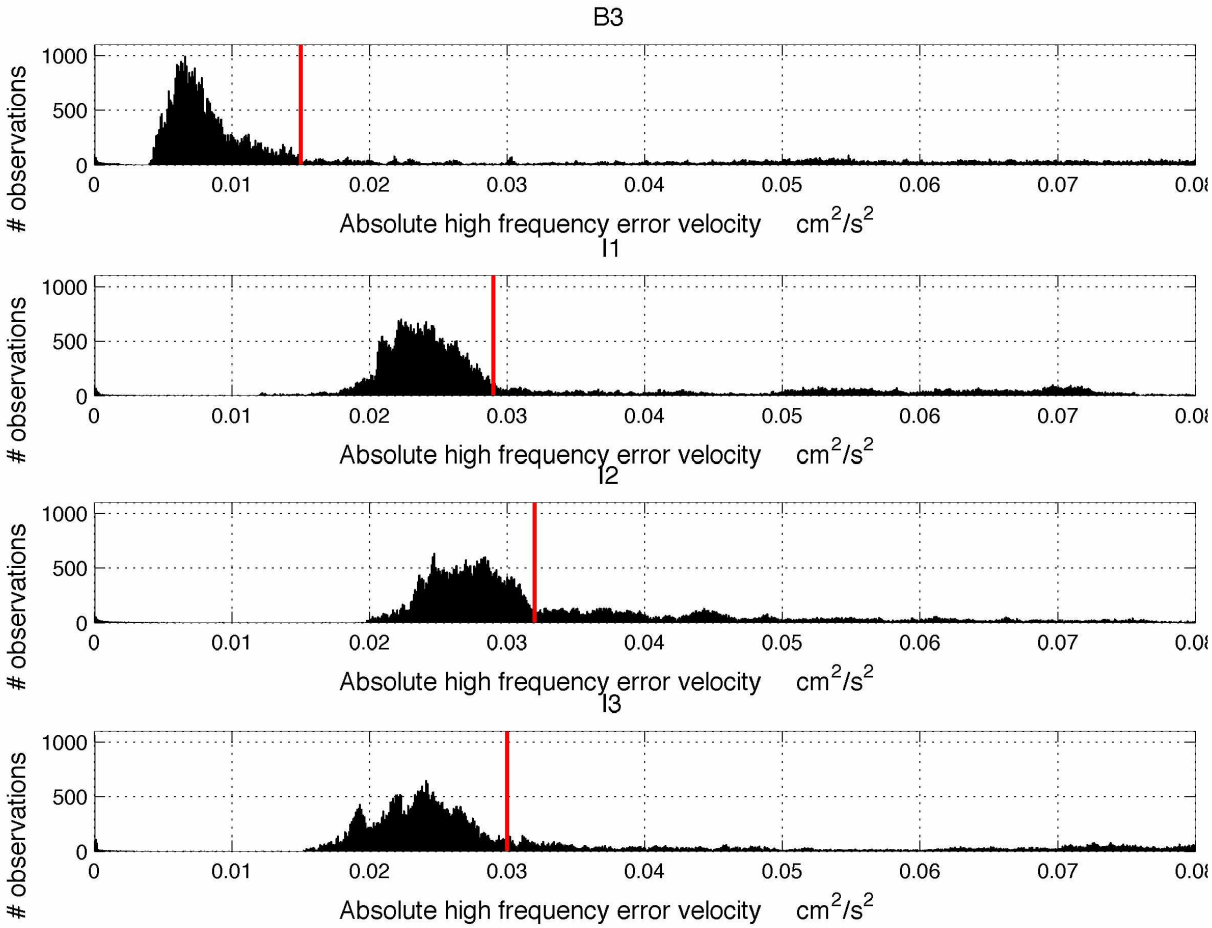

Figure 6: Histogram of the absolute value of error velocity for all moorings. The red bar indicates sea ice presence cutoff. The number of records indicates how often the absolute value of error velocity was observed at each mooring.

Two B3 hourly measurements were assembled to 2 h and 15 "I" mooring 8 min measurements were assembled to the same temporal resolution of 2 h. Using the ice presence product calculated earlier, non-ice times i.e., open water bottom track velocities, were rewritten as zero, while sea ice velocities were left untouched.

2.2 Sea ice concentration from the error velocity ice detection method

Daily sea ice concentrations were calculated based on the binary ADCP "ice" or "no-ice" ice time series of two-hourly data over a 24-hour period following the method of Visbeck and Fischer [1995] with some modifications. Ice presence or absence was tabulated as one or zero over the ensemble interval and a daily mean was calculated resulting in the percentage of ice observed over the mooring in a given day. All the moorings were examined individually and also assembled into a single time series that effectively covers approximately the same area of the satellite pixel. This method relies on the assumption that the ice was moving statistically the same way over a daily time period. Visbeck and Fischer [1995] found that this assumption was valid as long as the observed ice drift was below 50 cm s^{-1}; therefore, in regions of large ice drift the ice/no ice assumption may not be appropriate. There were no ice velocities above 50 cm s^{-1} in the ICORTAS moorings.

2.3 Rotary decomposition of current into clockwise and anticlockwise rotation

A Fast Fourier Transform was performed on the complex ADCP bottom track velocities for a running 3 d window in order to calculate the clockwise (CW) and counter-clockwise (CCW) rotary ice kinetic energy spectra [*Emery and Thomson*, 2001]. The near-inertial window was defined as +/- 10% of local f ($1.3e^{-4}$ s^{-1}-$1.5e^{-4}$ s^{-1}). The total power in this frequency range for the clockwise component of the signal was then integrated and stored as the "near inertial energy" (NIE) time series (Section 3.2).

2.4 Time domain estimate of inertial energy

For comparison to NIE time series, a complimentary time domain velocity time series of inertial currents (NIV) was identified by regressing the data to

$$u = A\cos(\frac{2\pi t}{T_1}) + B\sin(\frac{2\pi t}{T_1})$$

$$v = C\cos(\frac{2\pi t}{T_1}) + D\sin(\frac{2\pi t}{T_1})$$

over a sliding window of 13 h. This analysis looks at total velocity at the inertial frequency and

does not separate the signal into CW and CCW rotation. However, from the rotary spectral analysis (Section 2.3), the total CW signal in the NI band is one order of magnitude larger than that in the CCW signal so that the time domain near-inertial velocity and near-inertial spectral power contain approximately equivalent information (Section 3.2).

3.0 Results

3.1 Satellite and ADCP estimates of ice concentration

For approximately 200 days of the year the array was 100% ice covered; however, there were brief events where ice concentration fell typically by about 10%, lasting from three days to a week (Figure 7). Beginning in late September, error velocity values fell to 20% of the maximum as sea ice formation started. Brief periods of open water were observed in early October at all moorings; however, the timing varied, with open water observed first in I3 and I2, followed by I1, and then B3. Large values of error velocity (range of 0.4 $cm^2 s^{-2}$ for open water versus 0.1 $cm^2 s^2$) indicative of open water conditions were briefly observed at I3 and I2 in mid-November, and this signal was also present in I1 and B3 but weaker. Error velocity stayed relatively low, implying ice cover until early to mid-December, where spikes of relatively high values were observed in all moorings, suggestive of periods of open water. After December, error velocity decreased through the end of January as sea ice concentration increased. Slightly higher values were observed in I3 and I2. The mooring I1 showed an increase in error velocity about a week after I3 and I2. All moorings showed low error velocity after January until late February and early March, indicative of high sea ice concentration. During this time, I2, I1 and B3 showed increases in error velocity, possibly because of small scale fractures, but I3 did not show the same response. From April through late May, error velocity for all moorings showed a marked increase when compared with the earlier winter months as the melt season progresses. By the beginning of June, error velocity was much higher than the ice covered months, once again indicating open water.

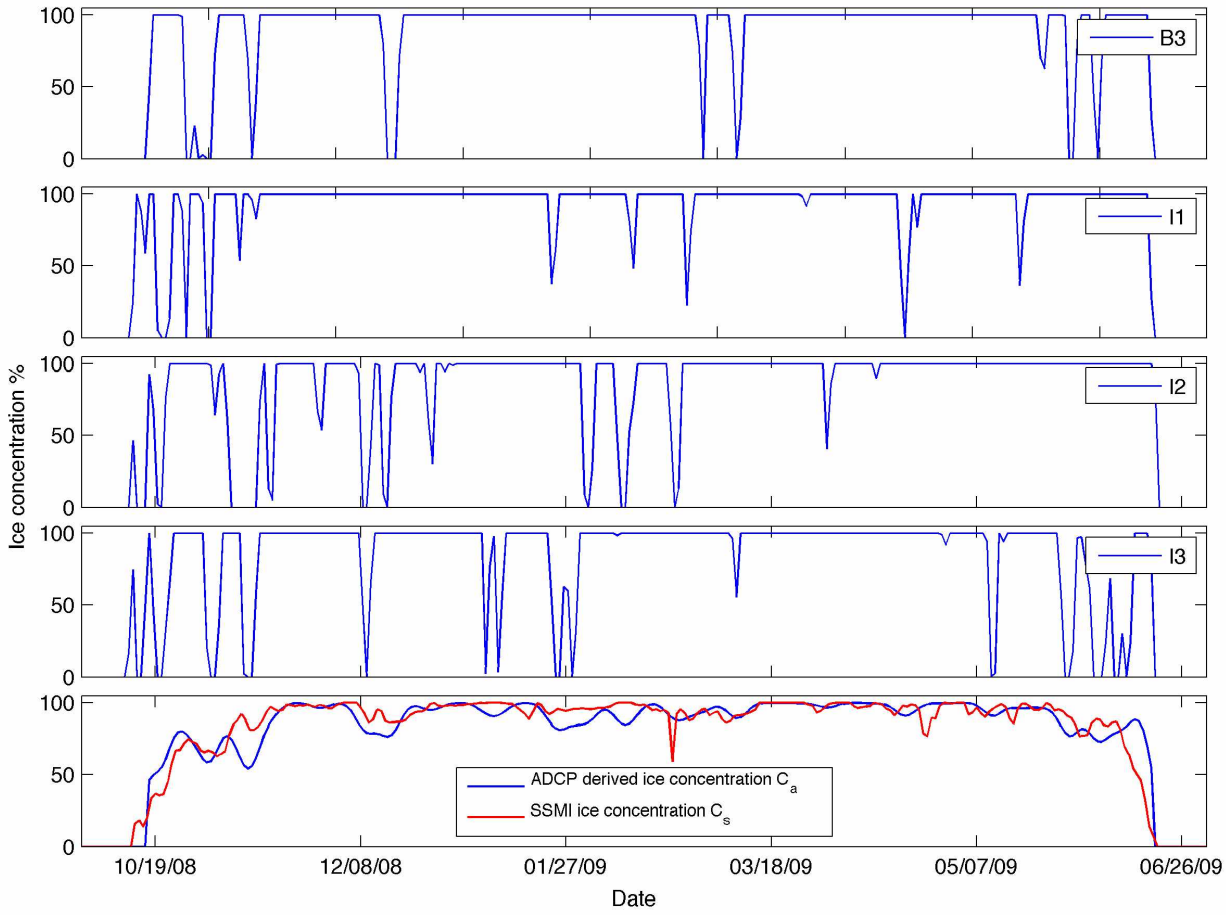

Figure 7: Satellite versus ADCP derived ice concentrations. Ice concentration from moorings B3, I1, I2 and I3 (panels 1-3). Ice concentration at the array site from the nearest SSMI pixel to I1-I3 (red) and a multi-mooring ensemble with ADCP-derived ice concentration (blue, C_A).

It was useful to examine the proxy ice-concentration derived from each individual ADCP record (Figure 7, panels 1-3) as well as a multi-mooring ensemble ice concentration proxy (C_A) to validate the sea ice detection scheme. At times the individual ADCP sea ice concentration time series showed differing estimates of sea ice concentration compared with the C_S data. However, averaging the individual ADCP records in both time and space created a dataset that agreed well with the C_A record. AVHRR skin temperature brightness imagery of 1.1 km resolution were scrutinized during an event starting on December 8th, 2008. Clouds obscured AVHRR skin temperature brightness imagery on this day; however, 2 days later they had cleared. Two moorings, I2, and I3 all showed 0% ice concentration but SSMI observed close to 100% ice coverage (Figures 8 and 9). AVHRR data suggested numerous large scale cracks in the region, some of which were greater than 100 km long and 5-10 km wide (boxed in Figures 10 and 11). While these cracks did not transit the mooring site, they were useful for estimating regional ice drift characteristics. During this time, sea ice velocities ranged from 1-10 cm s^{-1}, or O(1-10) kilometers of sea ice drift per day. This distance was below the nominal SSMI resolution of 25 km^2 x 25 km^2 (625 km^2). Over the course of 24 h, this open-water feature was tracked as it moved 30 km to the northwest. This also coincided with the reduction of sea ice concentration near shore and southeast of the array site, which unfortunately was blocked by clouds in the AVHRR skin temperature brightness dataset.

It was unsurprising that ice-concentrations were sensitive to the spatial scale considered. The 40 m^2 footprint of an individual ADCP resolves many features that may pass over the array but that SSMI (625 km^2 footprint) may not detect. Features with scales that were less than the distance between individual moorings can result in vastly different ice concentration estimates across the array. Likewise, features such as the decrease in nearshore ice concentration southeast of the mooring array were easily visible in SSMI but were not observed in the array even though this region abuts the array.

The multi-mooring ensemble estimate (C_A) of sea ice concentration temporally lead the satellite estimates (C_S) by about 5 d during freeze up (around Oct 10th), and showed higher values throughout winter (Figure 7). SSMI data are known to be biased and may under-predict ice coverage during the ice-forming period [*Willmes et al.*, 2013]. C_A roughly mirrored C_S, with a linear regression of R^2=0.86; however, there were times when they differed. C_S errors were

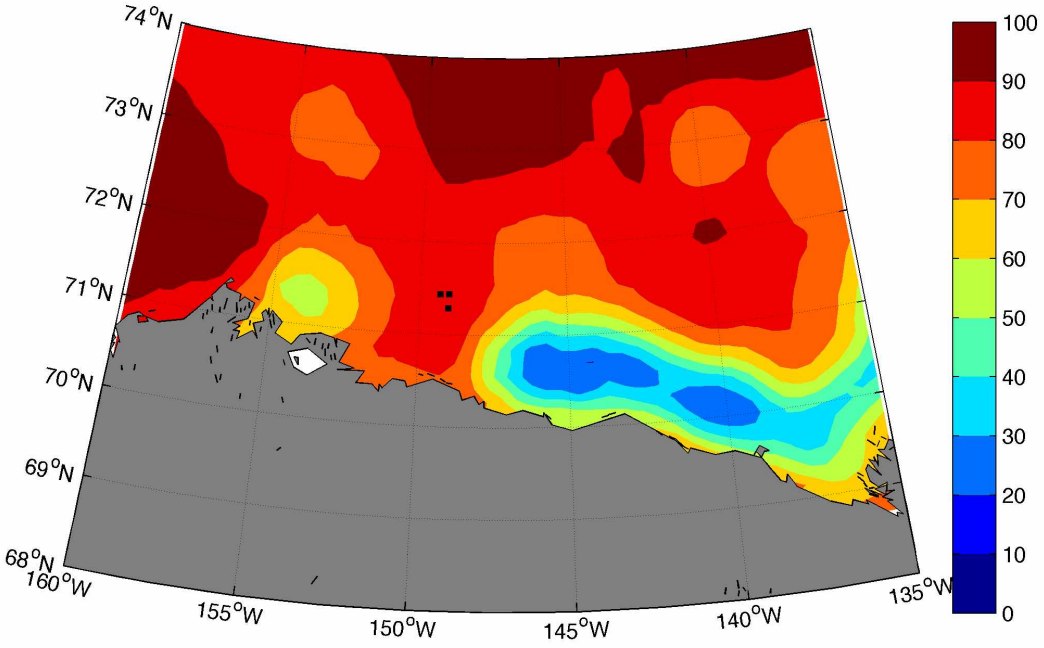

Figure 8: Satellite ice concentration example 1. SSMI ice concentration (%) on December 10th, 2008. Dots indicate the mooring array.

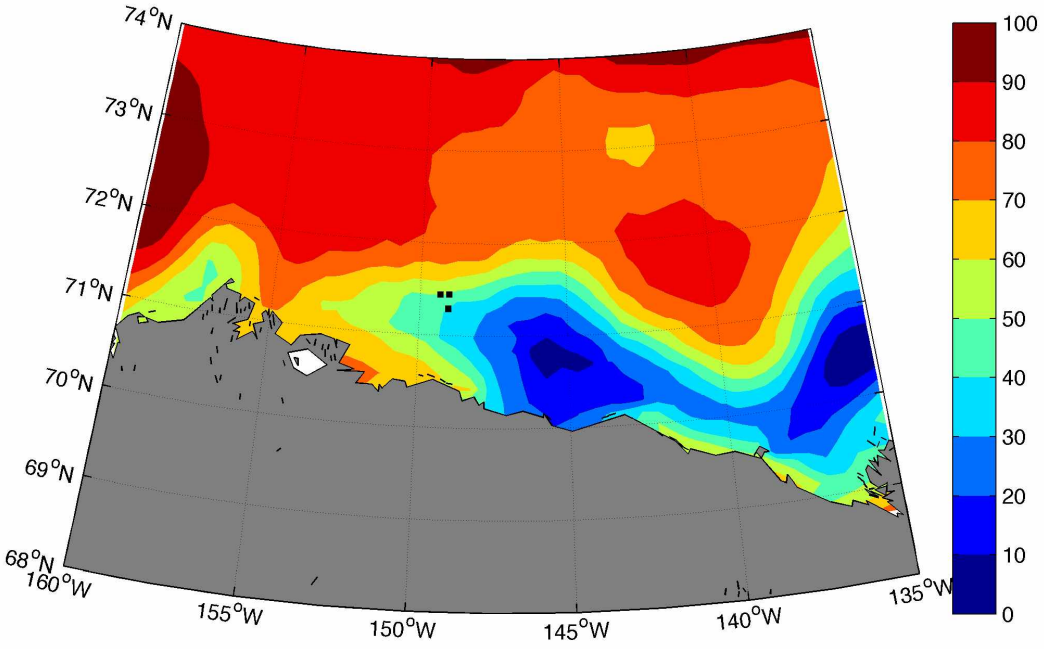

Figure 9: Satellite ice concentration example 2. SSMI ice concentration (%) on December 11th, 2008. Dots indicate the mooring array.

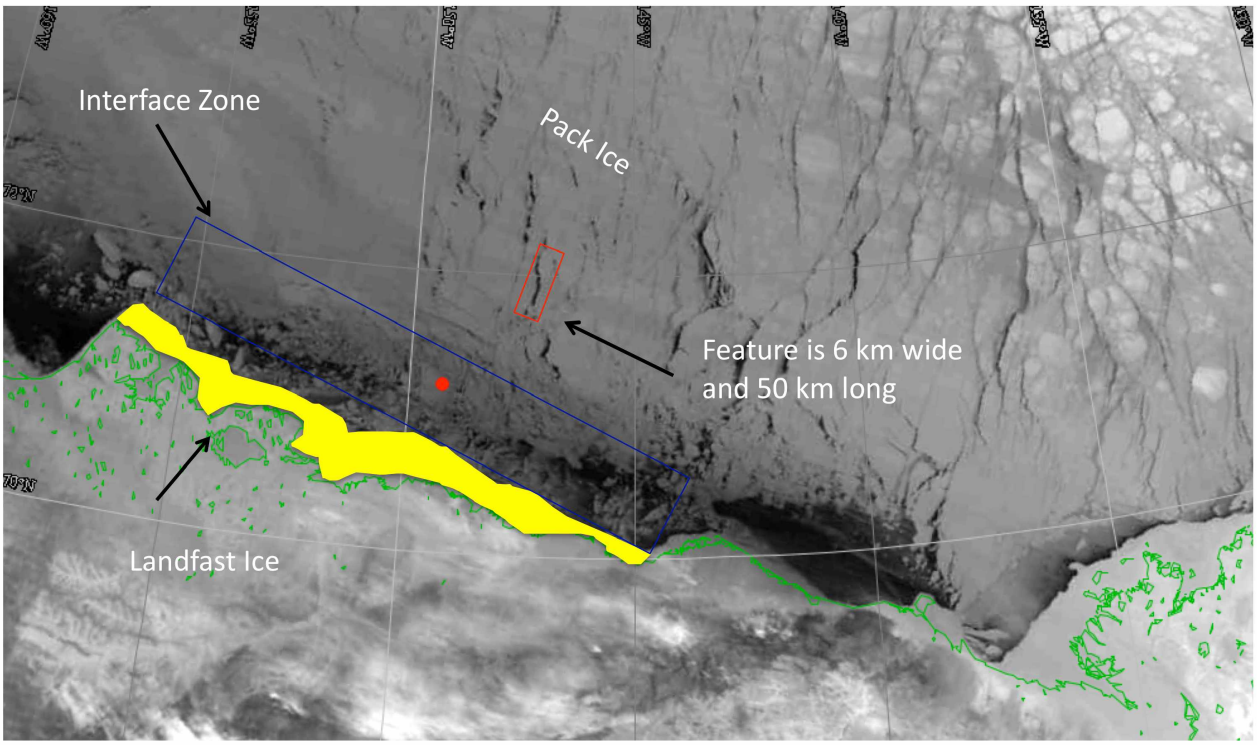

Figure 10: Satellite imagery example 1. AVHRR skin temperature brightness imagery on December 10th, 2008. The mooring array is indicated as a red dot.

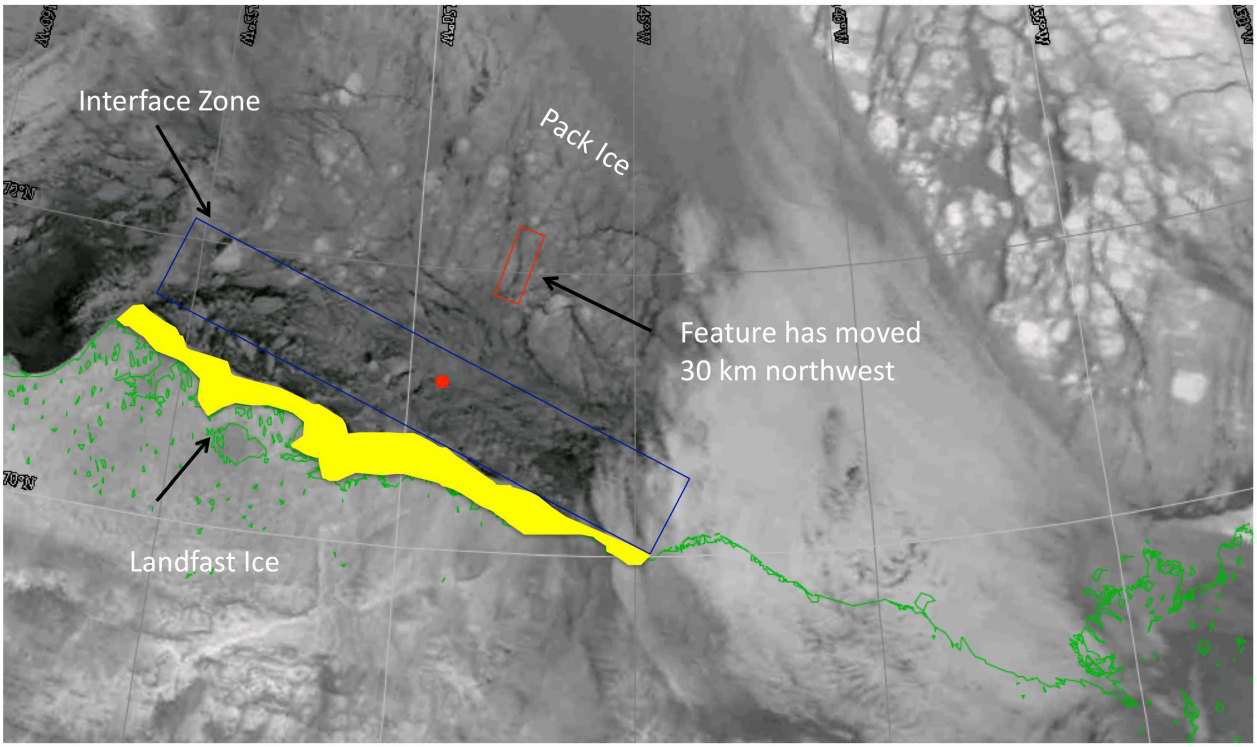

Figure 11: Satellite imagery example 2. AVHRR skin temperature brightness imagery on December 11th, 2008. The mooring array is indicated as a red dot.

difficult to quantify because the ice pack was constantly changing its physical and radiative properties. Sea ice emissivity changes throughout the year as ice formation progresses from nilas to multi-year ice. The SSMI bootstrap algorithm is optimized for thick first year ice, whereas areas of 100% newly formed ice are generally estimated to be as low as 80% due to lower emissivity [*Markus and Cavalierie*, 2000]. Meltponds in the summer also contribute to the observed bias. Comiso [1986] estimates SSMI accuracy to be 5-10% except during large fractions of thin ice and stormy weather conditions, especially near the ice edge. Armstrong and Brodzik [2002] also found that the SSMI snow and ice algorithm could underestimate values when observing bright surfaces. These adjustments were made to the bootstrap algorithm; however, it is not known if this affects the freeze up and melt time and the length of the ice covered season.

During the spring melt season, C_A lagged C_S by about a week, probably due to a bias in C_S whereby meltponds on the ice surface were identified as open water signal [*Willmes et al.*, 2013]. C_A showed a similar magnitude decrease in late October as SSMI, with C_A approximately 10% higher, probably due to the SSMI pixel integrating storm activity in its larger footprint. C_S values were about 30% higher until mid-November when they both reached close to 100%. In mid-December both C_S and C_A concentrations decreased by about 15% with C_A 3-5% lower than C_S, which was within the standard deviation of the SSMI bootstrap product. They then both recovered to 100% by the beginning of January. C_S then fluctuated between 90% and 100% for about 1.5 months beginning in late January and ending in early March when it recovered to 100%. C_A dipped down to 90% gradually beginning in late January and reached this value in early March; however, it did not fluctuate like C_S, which probably reflected the non-uniformity of sea ice properties over the satellite footprint. After early March, C_S dipped rapidly from 100% down to 60%, but recovered quickly to 95% till early April, when it jumped up to 100%. C_A fluctuated between 95% and 100% during this time, but reached the same value as C_S at the same time. For the month of April, C_S fluctuated between 95% and 100% while the C_A stayed at approximately 100%. In late April, both time series were approximately at 90%; however, the C_A increased back to 100% by early May, while C_S decreased to 78% and recovered back to 100% in early May again due to transient opening and closing within the SSMI footprint. After this period C_S fluctuated between 100% and 85% till early June when it dropped briefly below 80%, then returns to 90%, after which it declined to 0% by the end of June. C_A fluctuated in phase

with the SSMI during this time; however, the magnitude of change was less since C_A was not biased by ice ponds on the surface. The brief recovery at the end of June was mirrored in C_S; however, C_A took approximately one week longer to start to descend to 0%, once again likely due to meltpond bias causing SSMI to spuriously report open water prematurely.

3.2 Time series analysis

Figure 12 summarizes the sea ice drift statistics, excluding ice-free conditions. Each mooring reflects the long-term mean ice drift of the Beaufort Gyre with measured sea ice drift predominantly westward. For all moorings there was a westward drift less than 20-30 cm s^{-1} 10% of the time. Occasionally, there were bursts of speed over 30 cm s^{-1} in a westward direction but they only amounted to 5% of the observed drift. Moorings B3, I1 and I2 showed slow ice drift directly to the north of up to 10 cm s^{-1} for 10% of the time. I3 showed the largest occurrence of this with a slow ice drift directly to the north 20% of the time. Ice floes at I2 did not drift directly north, but rather to the northeast for approximately 15% of the time, with drift velocities under 10 cm s^{-1}.

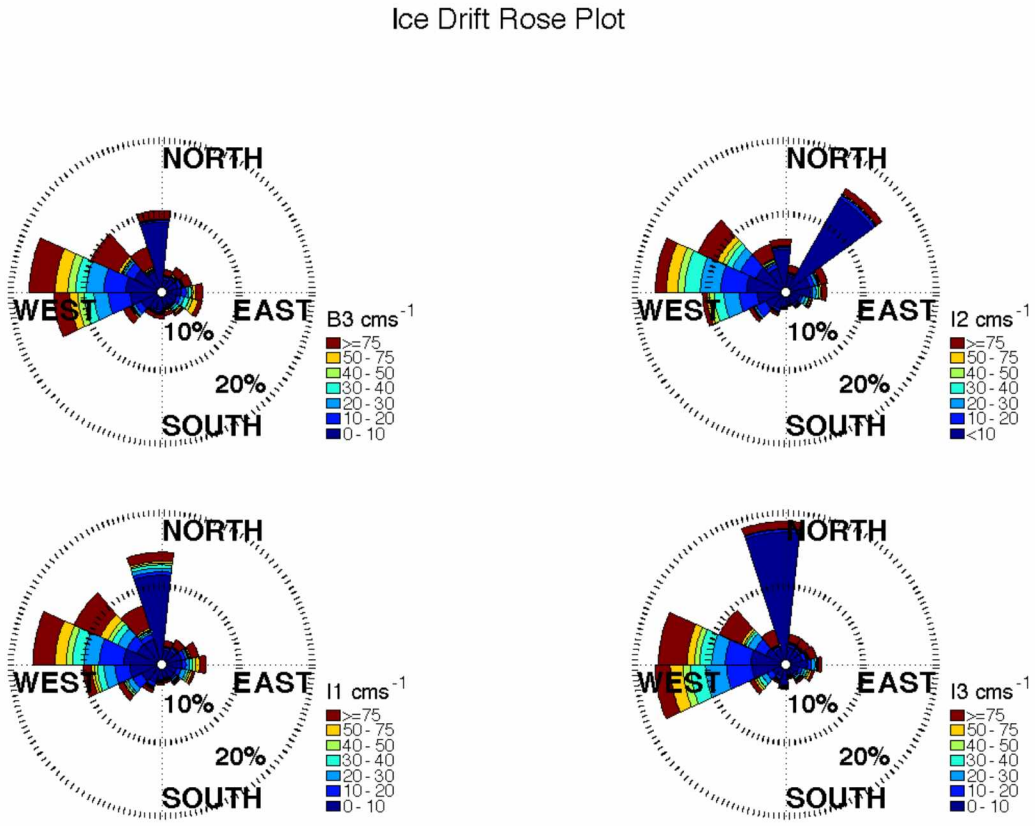

Figure 12: Ice drift rose plot. Rings indicate the percentage of time ice was drifting in that direction. Colors indicate magnitude and the relative proportions of the colors indicate how often that magnitude was observed.

Frequency spectra of ice velocities were calculated. The ice velocity CW spectrum was blue, with variability dominated by low frequencies (Figure 13). A peak stands out near the Coriolis frequency in the CW component. This indicates that the ice moved clockwise more often than it moved counterclockwise near the Coriolis frequency, consistent with a signal dominated by near-inertial oscillations in the northern hemisphere. The time series of maximum near inertial power (Section 2.4) was plotted versus the multi-mooring ensemble ice concentration (Figure 14). Two high, near-inertial ice energy events in December and February, both of which corresponded to dips in ice concentration, were examined in greater detail in section 3.3. Reduced or diverging ice may allow large near-inertial oscillations during these events, while converging ice and high ice concentration may damp them. In comparison, the inertial currents were less than 1 cm s^{-1} during non-event times; however, an increase up to 20 cm s^{-1} was observed during the largest observed event in December, with other event values ranging from 5-15 cm s^{-1}.

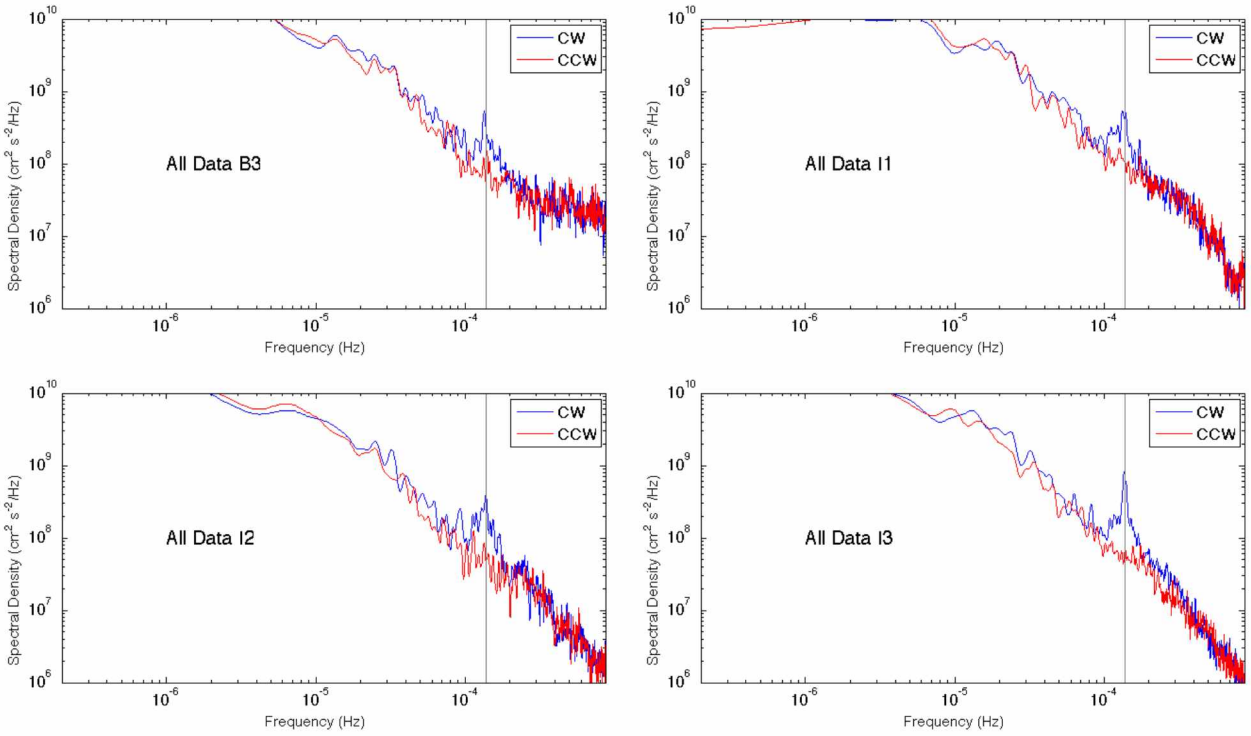

Figure 13: Rotary spectra. Clockwise (CW) and counter-clockwise (CCW) ice kinetic energy spectra .The x-axis is frequency in Hz and the y-axis is spectral power in cm^2 s^{-2}/Hz. The grey line denotes the Coriolis frequency at this latitude.

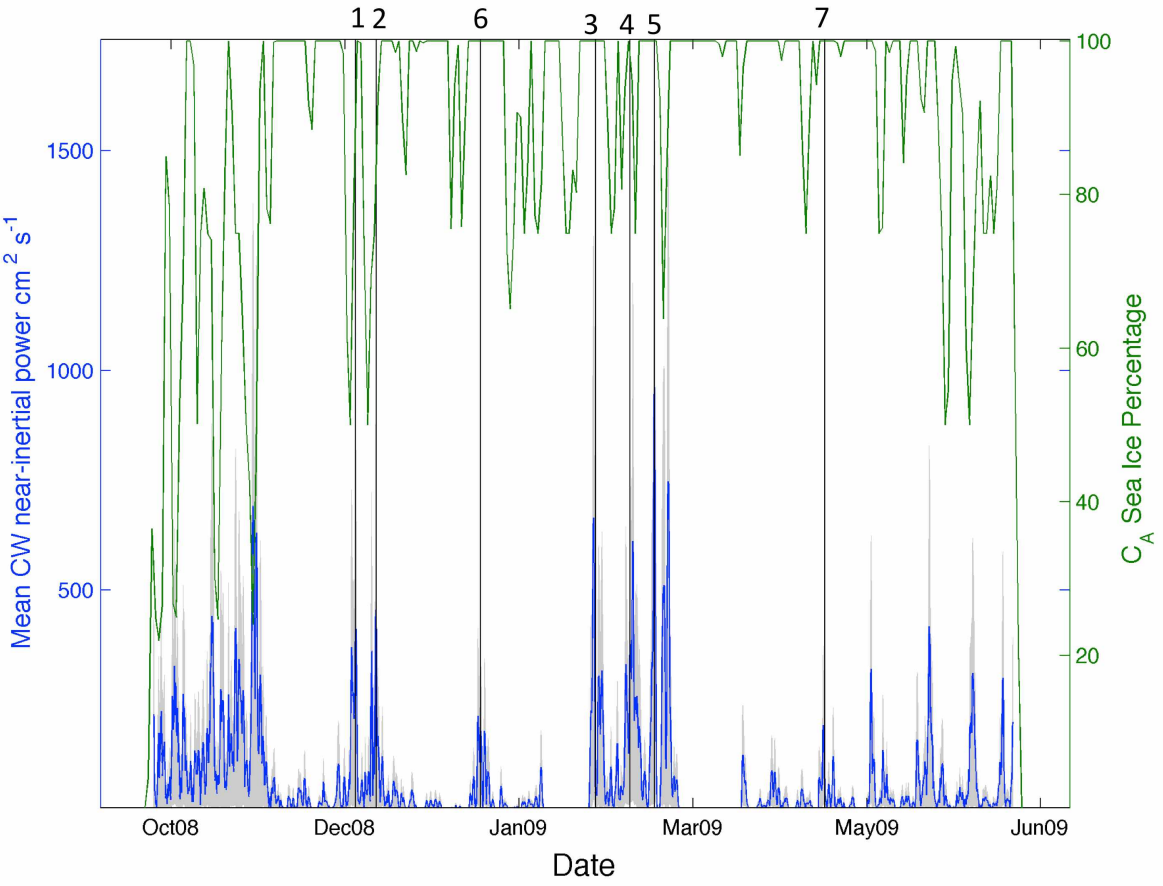

Figure 14: Near-inertial time series. Local clockwise (CW) near-inertial power velocity time series for all moorings (blue line) and multi-mooring ensemble (green line, C_A) ice concentration. The grey line indicates the scatter in inertial power among moorings. Seven individual events are labeled.

Calculating the divergence over the mooring array provides a measure of how the ice pack was able to open and thus allow mechanical energy to transfer from the atmosphere into the ocean. To calculate divergence a total derivative with only horizontal components was calculated between all "I" moorings every 2 h (note: this calculation did not include the mooring BS3). The number was defined by measuring the change in velocity between each mooring divided by the distance between moorings on a Cartesian plane, where total derivative=du/dx+dv/dy. du and dv were calculated as the velocity differences between moorings pairs while dx and dy were calculated as the x and y distances, respectively. Divergence was calculated for each mooring pair, and then all pairs were summed together for our proxy divergence estimate. The area of the smaller enclosed triangle (moorings I1-I3) shown in Figure 3 was 54.7 km^2 (note: this was smaller than the 91.7 km^2 area compared to the SSMI pixel) and the mean distance between moorings was 11.7 km. A reduction in satellite sea ice concentration was observed when divergence went up, suggesting that the mooring derived divergence was large enough to influence the SSMI pixel (~twice the size of the mooring enclosed area), thereby confirming likely conditions for sea ice to move freely in response to the wind. Interestingly, the spectra of ice divergence showed an increase near the Coriolis frequency (Figure 15), consistent with Hibler et al. [1974].

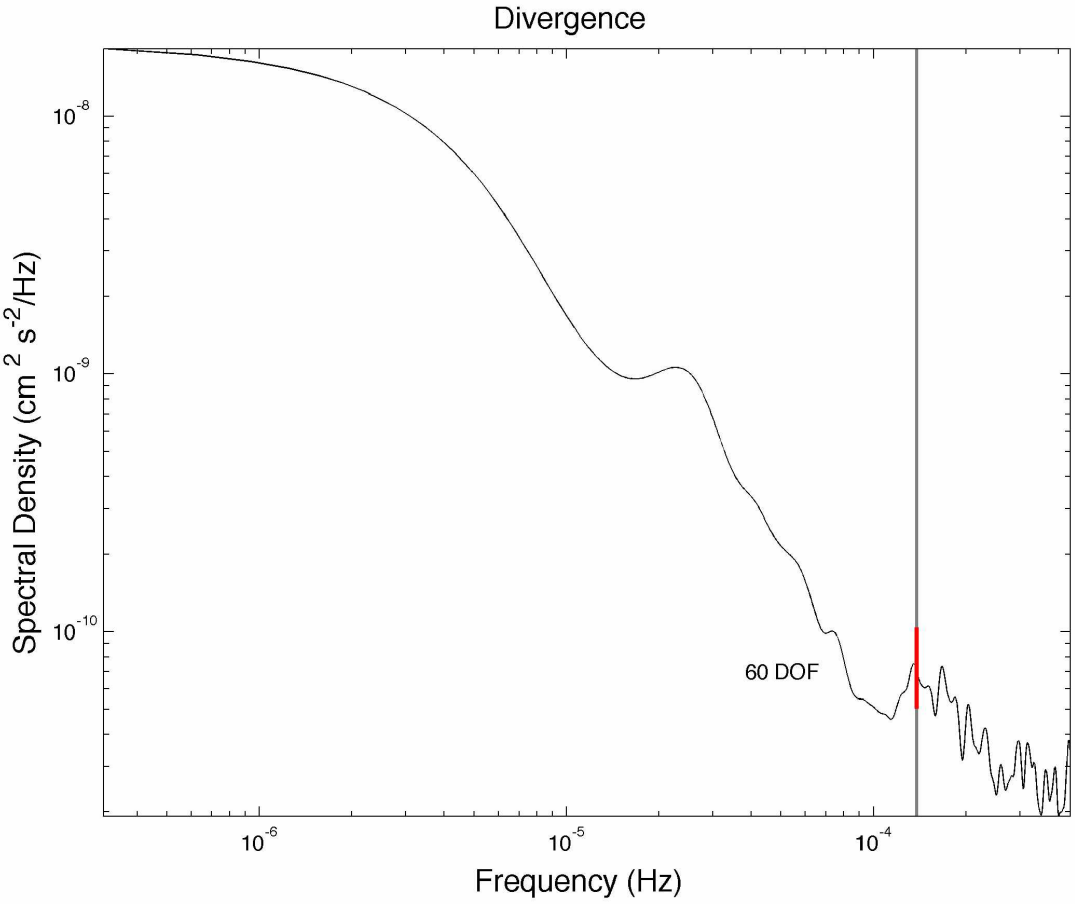

Figure 15: Divergence spectra. Smoothed divergence spectra of all "I" moorings (60 Degrees of Freedom). The red line indicates the error bar and the grey line denotes the Coriolis frequency at this latitude.

3.3 Storm event case studies

A total of seven storm events during the winter of 2008-2009 were studied for their impact on near-inertial sea ice motions. Two events showed high levels of near-inertial energy that corresponded with weather systems that either moved quickly or were the proper diameter, while the other five were associated with systems that either moved slowly or had a larger diameter. It was found that atmospheric system time and space scales along with sea ice deformation (inferred from divergence) were a strong predictor of near-inertial sea ice response. Table 1 contains the parameters of each storm event below.

Table 1: Storm timescales.
Summary of seven storm event parameters and sea-ice response characteristics.

Event #	**Date**	**Diameter km (D)**	**Ground track Velocity m/s (U)**	**D/U**	**Notes**
1	12/09/08 – 12/11/08	573.5	37.4	15.4	Winds fell quickly. Small inertial response observed
2	12/14/08 – 12/19/08	615.8	60.9	10.1	Large inertial response. Evidence of preconditioning from storm 1
3	2/15/09 – 2/18/09	706.7	75.1	9.4	Similar to December event #1, acted to precondition.
4	2/25/09 – 2/27/09	650.9	63.2	10.3	Instead of a low pressure system, this was a high pressure system.
5	3/7/09 – 3/9/09	573.5	37.5	15.3	Another high pressure system. Winds stopped then reversed.
6	1/14/09– 1/18/09	715	22.2	32.2	Weak inertial response
7	4/26/09– 4/28/09	1669.8	50.3	33.3	Weak inertial response

Two storm events in particular excited unusually energetic near inertial responses in the sea-ice cover, one starting in mid-December 2008 (events 1 and 2, Figures 16-18) and one starting in late February/early March 2009 (events 3,4, and 5, Figures 19-22). Both of these events were accompanied by winds that changed direction quickly over an inertial period, characteristic of fast moving storms that were relatively small in diameter. Furthermore, both events consisted of smaller mini-events, where analysis of ice-divergence over the array suggests that the initial event acted to precondition the ice pack, allowing more near-inertial response for the following events. Two events that produced weak inertial responses were also examined (events 6 and 7). Both of these events had slow moving, large diameter storms accompanied by winds that changed directions slowly.

3.4 December event 1

On the night of December 7, 2008 at 1600 hours, the Barrow winds were from the southeast at 3 m s^{-1} (Figure 16d). They steadily strengthened until they reached a maximum of 5 m s^{-1}. At 0400 on December 9th the winds suddenly fell and by 1800 they were out of the northeast at 3 m s^{-1}.

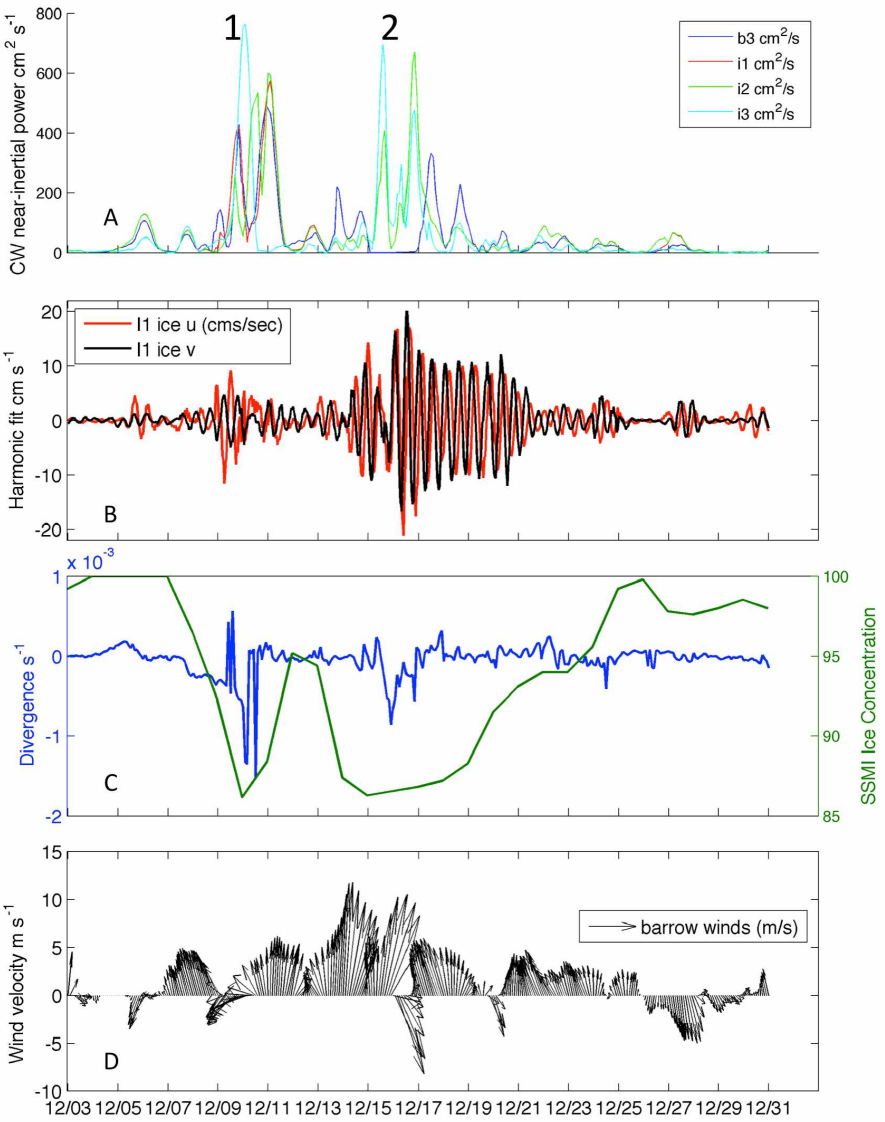

Figure 16: December event composite. A composite of near-inertial ice energy (panel A), inertial currents (panel B), ice divergence and concentration (panel C), and Barrow wind velocity (panel D) during December 2008.

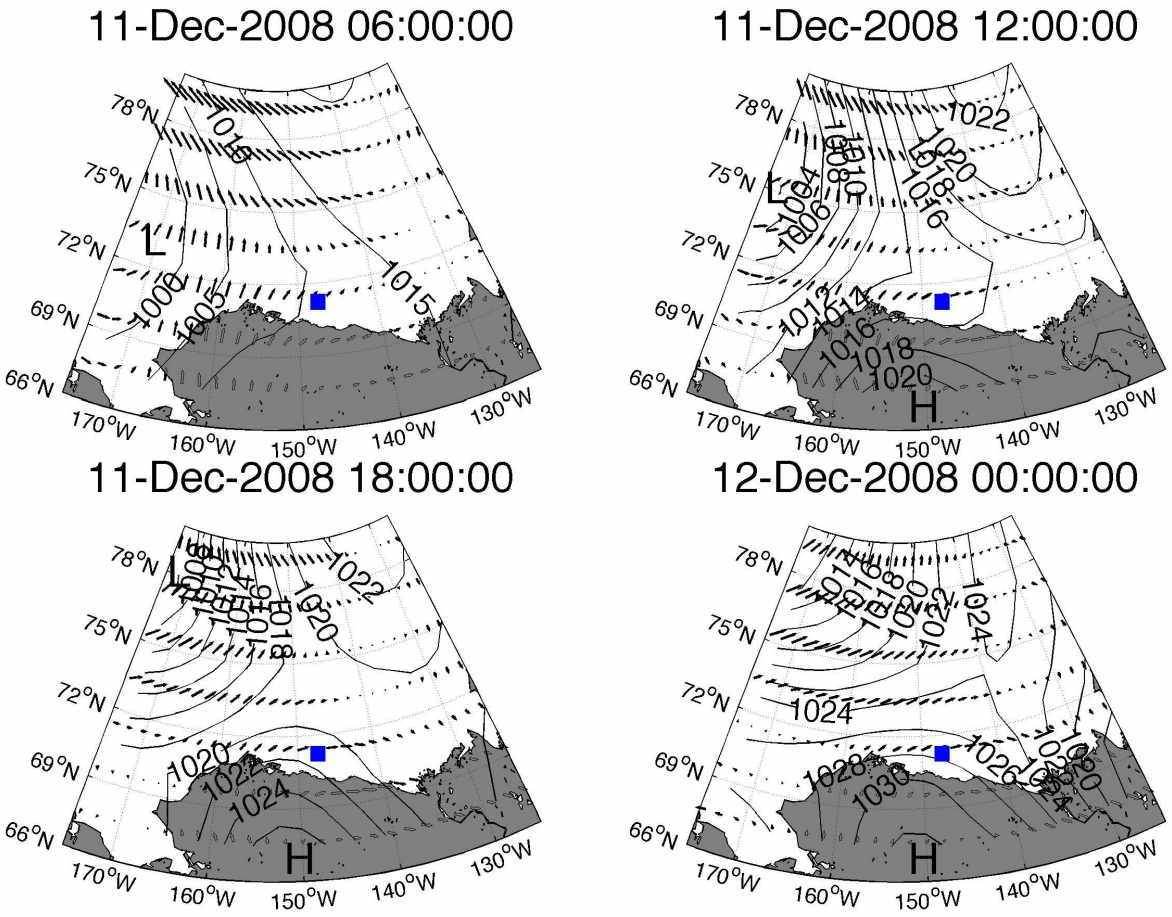

Figure 17: December sea level pressure and wind map for event 1. The ICORTAS mooring array location is indicated by the blue square.

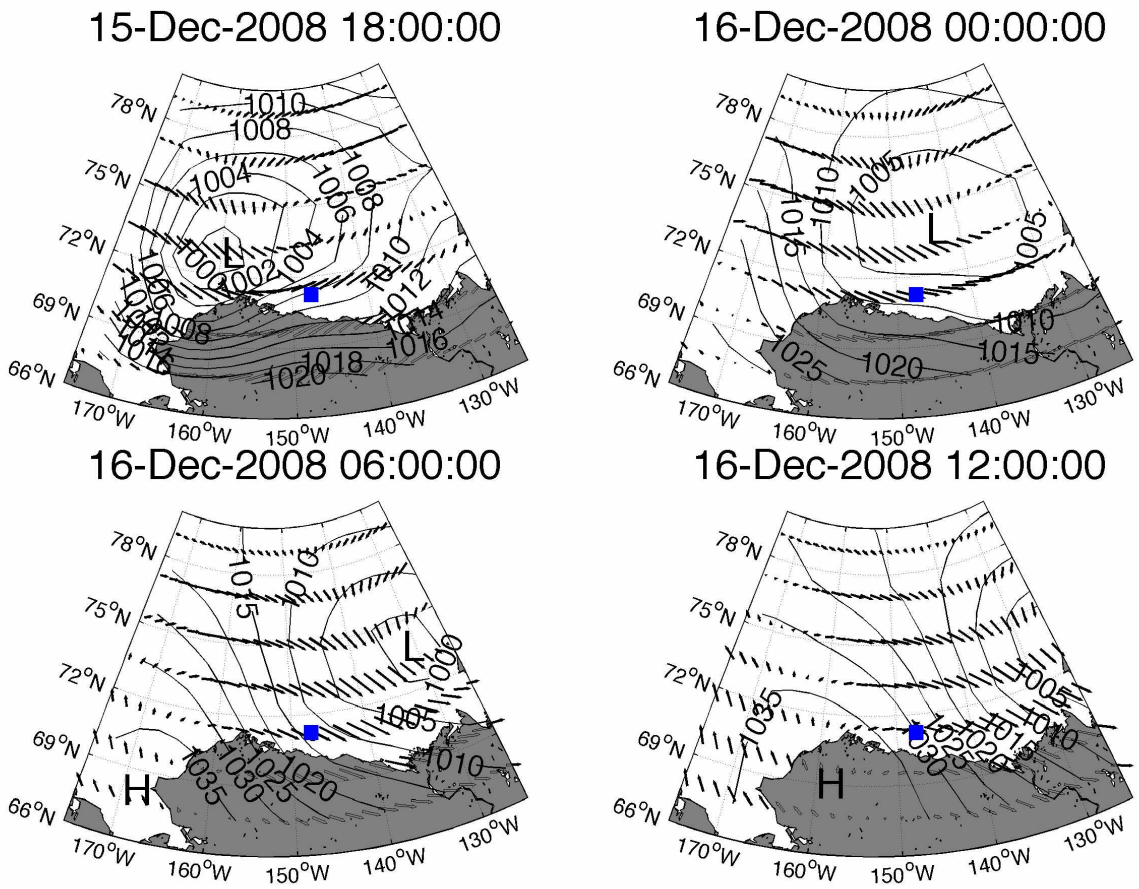

Figure 18: December sea level pressure and wind map for event 2. The ICORTAS mooring array location is indicated by the blue square.

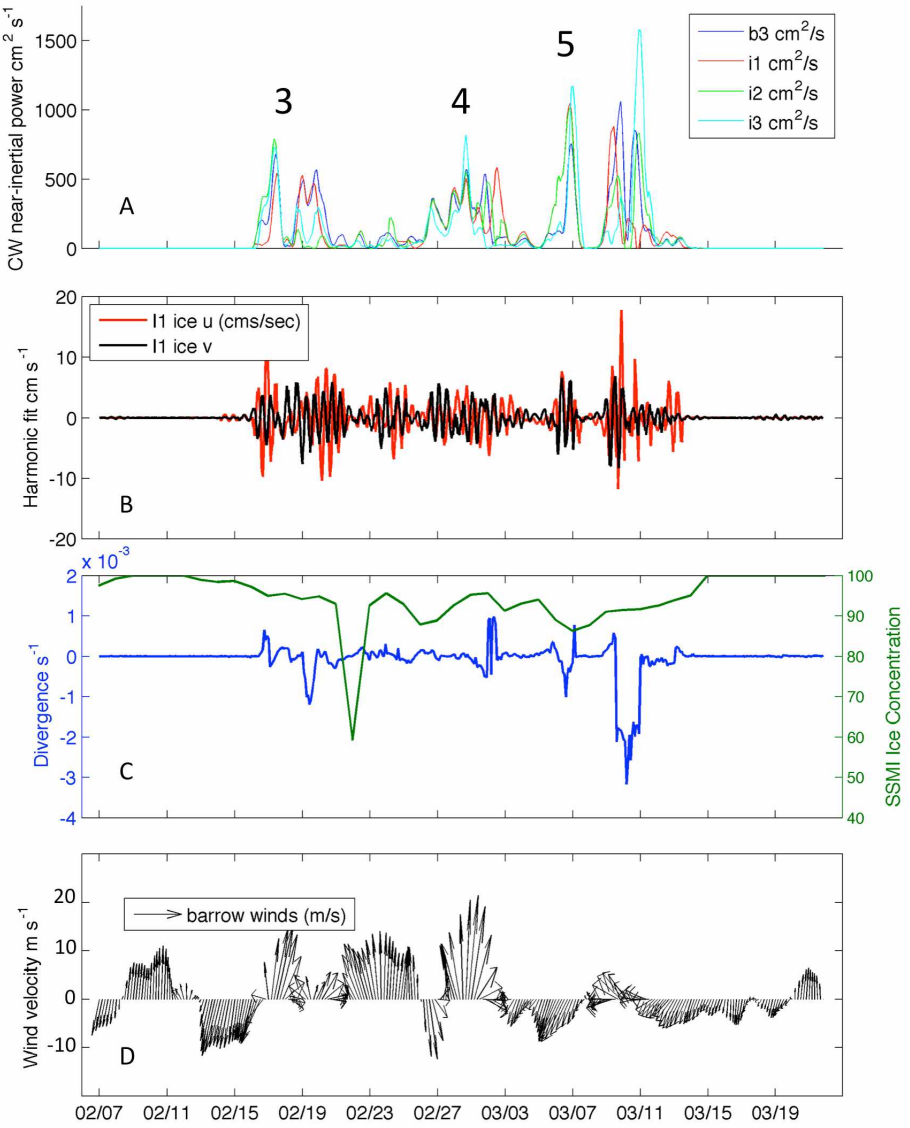

Figure 19: February event composite. A composite of near-inertial ice energy (panel A), ice velocity harmonic fits (panel B), ice divergence (panel C), and winds (panel D) during high levels of near inertial energy observed in February 2009.

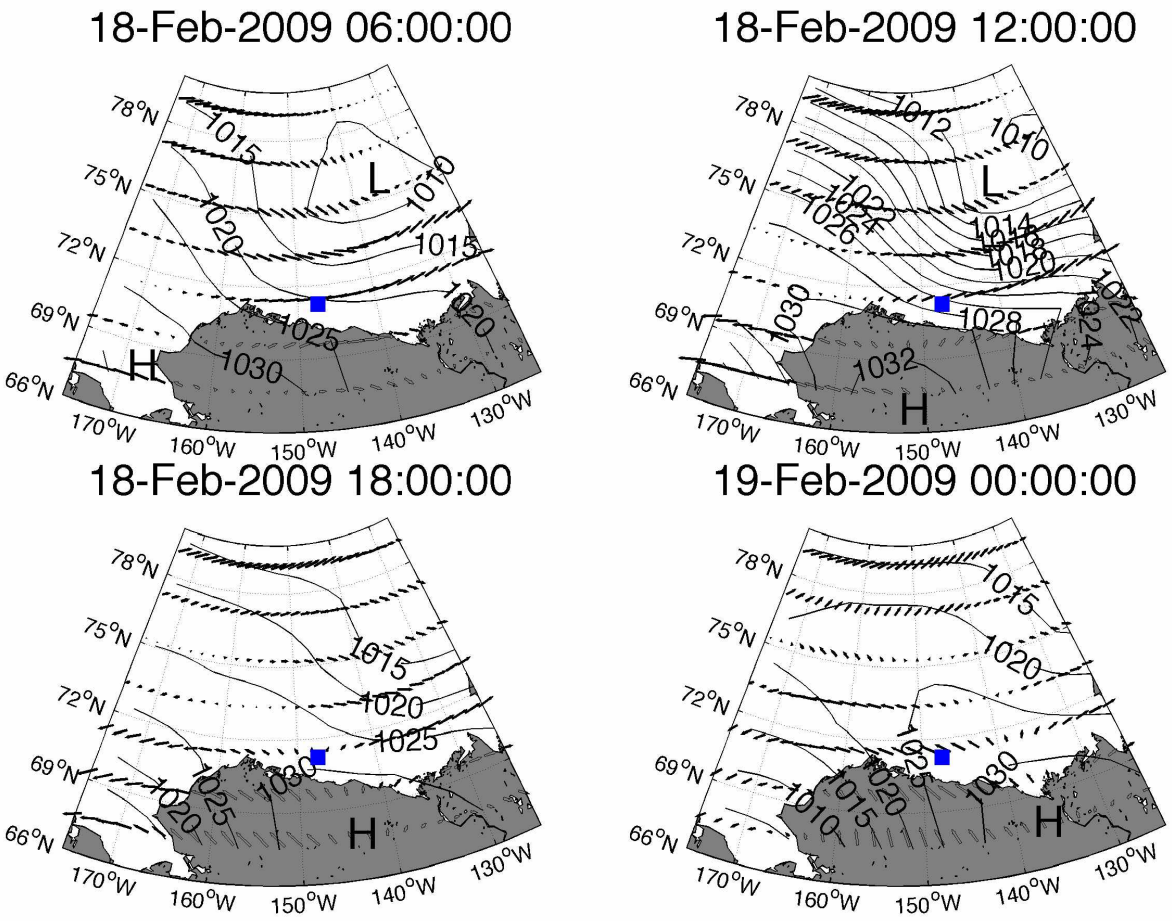

Figure 20: February sea level pressure and wind map for event 3. The ICORTAS mooring array location is indicated by the blue square.

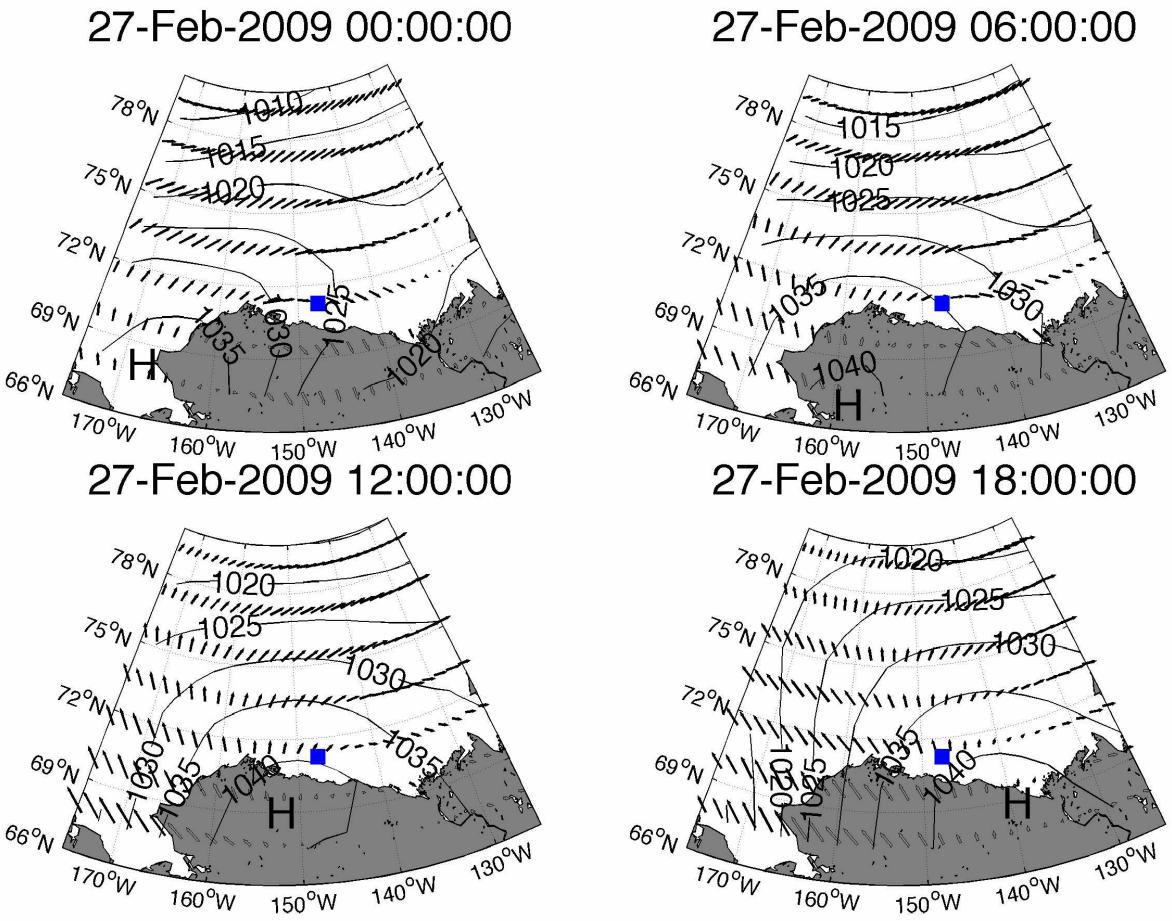

Figure 21: February sea level pressure and wind map for event 4. The ICORTAS mooring array location is indicated by the blue square.

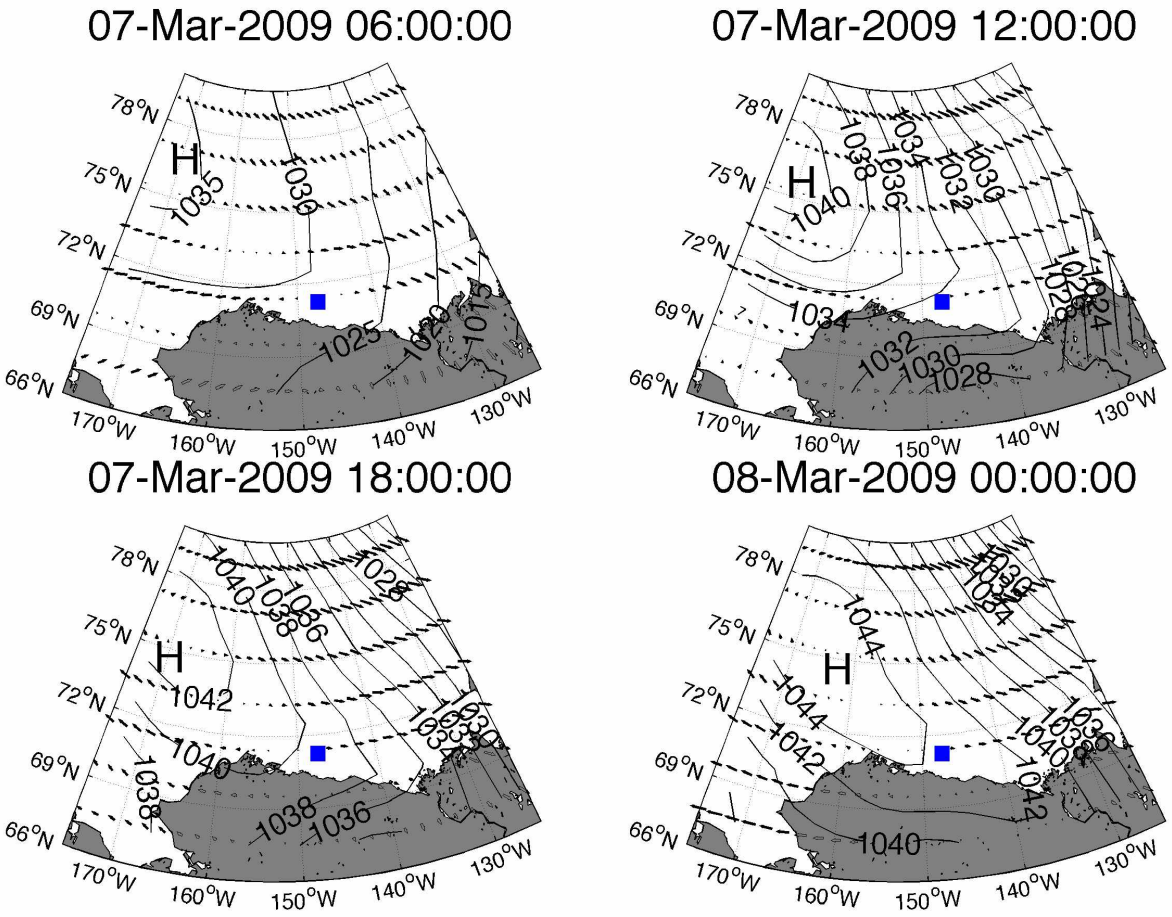

Figure 22: March sea level pressure and wind map for event 5. The ICORTAS mooring array location is indicated by the blue square.

National Centers for Environmental Prediction (NCEP) reanalysis showed a low pressure system located over the western Chukchi Sea on the night of December 9th that caused southerly winds over the mooring array (Figure 17). As the day progressed, the low-pressure system tracked farther north and a high pressure system moved from interior Alaska to a position centered over the North Slope of Alaska over land. By December 10th at 0000 hours, winds over the mooring array shifted until they were completely out of the east (Figure 16d). Twelve hours later the low-pressure system moved even farther north while the high-pressure system remained fixed, shifting the winds over the mooring array to the northwest. This was the event that caused the first sea ice near-inertial response, event 1. A rise in the clockwise near-inertial sea ice energy was observed with the strongest response at the shelf mooring I3. A decrease in the sea ice divergence from positive to negative was observed over the triangular region encompassing I1, I2 and I3. There was a corresponding rise in near-inertial energy (Figure 16a) with corresponding inertial-band ice velocity fluctuations reaching 10 cm s^{-1} (Figure 16b). Over the next 24 h the wind slowly switched direction so it was from the South by 0000 on December 11th. Sea ice near-inertial energy was damped within 3-4 cycles (~24-36 h). Satellite ice concentration also decreased from 95% before the event to 85% after the event. This event may have preconditioned the ice pack for the next event observed 3 days later, which was considerably stronger.

3.5 December event 2

Event 2 followed immediately after event 1, and the large sea-ice response resulting from the storm may have been a result of weakened sea-ice and reduced concentrations resulting from event 1. Winds were sustained from the south at 5 m s^{-1} for these 3 days until December 13th at 0600 when over the course of 16 h until 0000 December 14th Barrow winds strengthened from the south at 10 m s^{-1}. A smaller rise in near-inertial energy compared to the initial event was observed, which may help prime the ice pack for the largest part of the event. Starting 0600 on December 15th the winds decreased over 18 h until the early morning of December 16th (Figure 16d). The highest amount of near-inertial energy for this event 2 was observed during this time. The inertial currents increased to +/- 20 cm s^{-1}. Over the course of a day the winds rotated to a northwesterly direction on the morning of December 17th, reaching a maximum of 6 m s^{-1}. After 2 days anti-cyclonic power was no longer observed, and 4 days later the inertial currents decayed to zero. NCEP reanalysis showed a strong (995 mb) low pressure system located in the eastern

Chukchi Sea that quickly moved to the east causing southwesterly winds over the mooring array on the night of December 15th (Figure 18). Six hours later the low had progressed into the Beaufort Sea while a high pressure system moved northwards from the Bering Strait and over the Seward Peninsula, shifting the winds from southwest to the west. As the low tracked further to the east and the high moved farther north, the winds shifted rapidly over 12 h until they had completely shifted from the southwest to directly north. Sea ice divergence also decreased although not as strongly as the previous event. Satellite ice concentration decreased from 92% to 85%.

3.6 February events 3, 4 and 5

Starting at 1200 February 15th, the winds were from the northeast at 5 m s^{-1}, then they changed 180° over the course of the next 1.5 days so that by 0000 February 17th they had switched to the southwest at the same magnitude (Figure 19d). A small rise in near-inertial energy (event 3) was observed. NCEP reanalysis showed a low pressure system in the middle of the Beaufort Sea on the morning of February 18th (Figure 20), which caused the wind shift. This low pressure system moved rapidly to the east due to a high pressure ridge, which developed over eastern Siberia and also propagated eastward. Sea ice divergence first increased and then decreased during that time as expected from a low pressure system, and a 20% drop in sea ice concentration in the satellite pixel was observed. This event acted similarly to the first December wind reversal, the effect of which was to precondition the ice pack so that subsequent wind reversal events had a greater effect. CW kinetic energy increased with all moorings showing similar CW near-inertial power. Associated inertial currents reached 10 cm s^{-1}. Sea ice oscillations were dampened within 48 h after 4-5 oscillations. From 0000 on February 26th to 1600 on March 1st, the winds slowly decreased from 5 to 2 m s^{-1} from the south. From 0000 to 1200 on February 27th, the wind velocity changed quickly over 6 h to 7 m s^{-1} directly out of the north (event 4). Reanalysis pressure data (Figure 21) showed a high located over the southern Chukchi/Beaufort boundary, causing winds from the north at the mooring site. This high moved rapidly to the east so that 16 hours later it had already traversed the entire state of Alaska and moved over the Mackenzie River Delta. The mooring I3 showed the largest increase in near-inertial sea ice energy; however, all moorings showed a response. Inertial currents reached 7 cm s^{-1} (Figure 19b). Divergence first decreased, then increased, as expected from a high pressure system, and a small drop in satellite ice concentrations was observed. Event 4 was unique

because it was a high pressure system that caused a near-inertial response, not a low pressure system. Another high pressure system starting at 0000 on March 7th also caused a similar response (event 5). This system caused the winds to drop to zero between 1200 and 1600 on March 7th and reverse direction by March 8th at 0600 (Figure 22). Sea ice near-inertial energy increased when the winds ceased and decreased as they picked back up. An increase in divergence was also observed similar to the other high pressure event 4.

3.7 January event 6

A slow moving low pressure system propagated in a northeasterly direction about 200 km north of Barrow with a center of 985 mb (Figure 24) starting at 1200 on January 16th. Winds were about 2 m s^{-1} from the northeast at Barrow (Figure 23d). Over the next 24 h the winds weakened and reversed direction to the southwest at the same speed as the low moved eastward and away from the array at 1200 on January 17th. Surprisingly, all four moorings showed similar rises in near-inertial energy; however, this amount of energy was only 1/10th of the energetic December event (Figure 23a). The inertial currents at I1 reached 7 cm s^{-1} (Figure 23b) and divergence went down by about 1 e^{-4} s^{-1} (Figure 23c), then fluctuated between zero and negative as the event progressed. This low amount of convergence, combined with a slight simultaneous rise of near-inertial energy at all moorings strongly suggests that the ice pack was moving as a coherent unit between the mooring array and was unable to overcome the internal ice pack strength and fracture. Contrasted with the previous events, the energy transferred from the atmosphere was enough to overcome these mechanics and fracture the pack as witnessed by the fluctuating divergence and near-inertial energy rise observed during the large near-inertial response events.

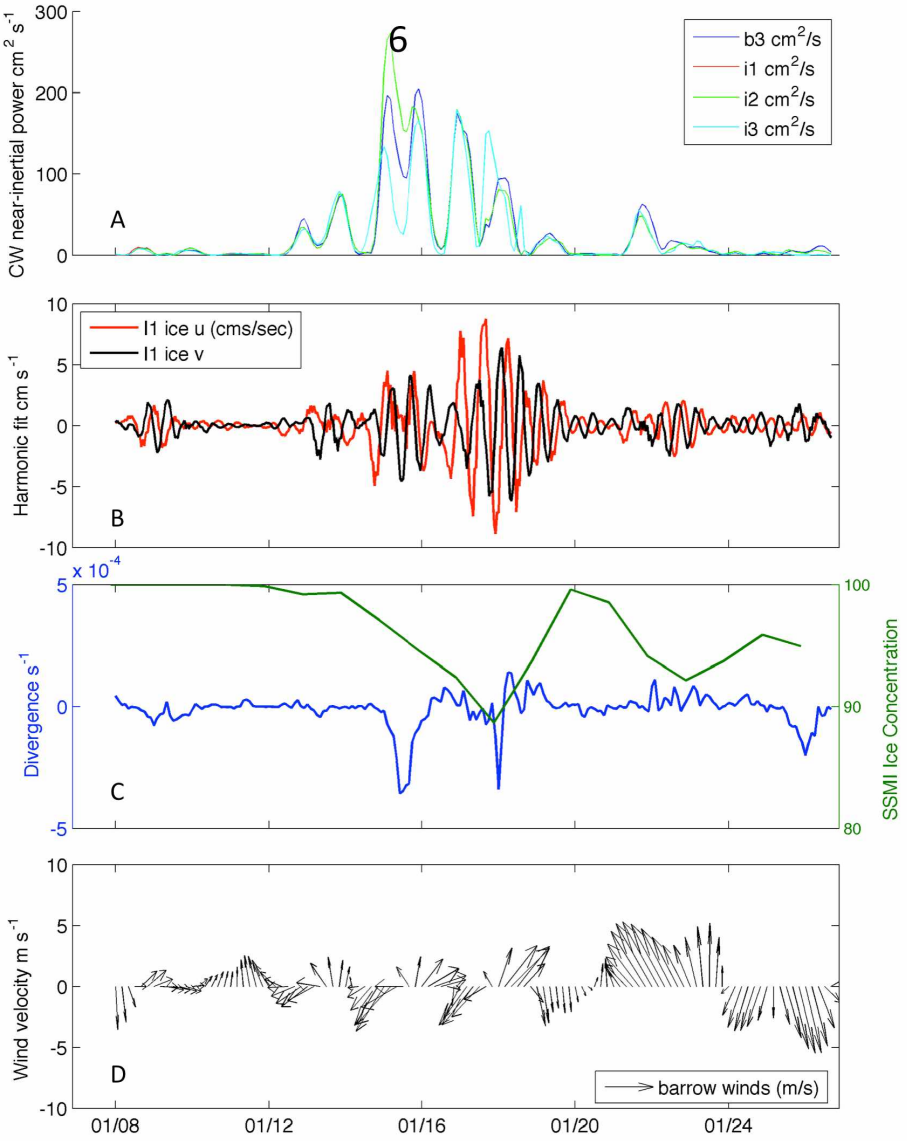

Figure 23: Low near-inertial power synthesis event 6. Storm event 6 composite of near-inertial ice energy (panel A), and ice velocity harmonic fits (panel B), ice divergence (panel C), and winds (panel D) during low levels of near inertial energy observed in January 2009. Note that vertical range of spectral energy and velocity plots are 1/10th that of Figure 16.

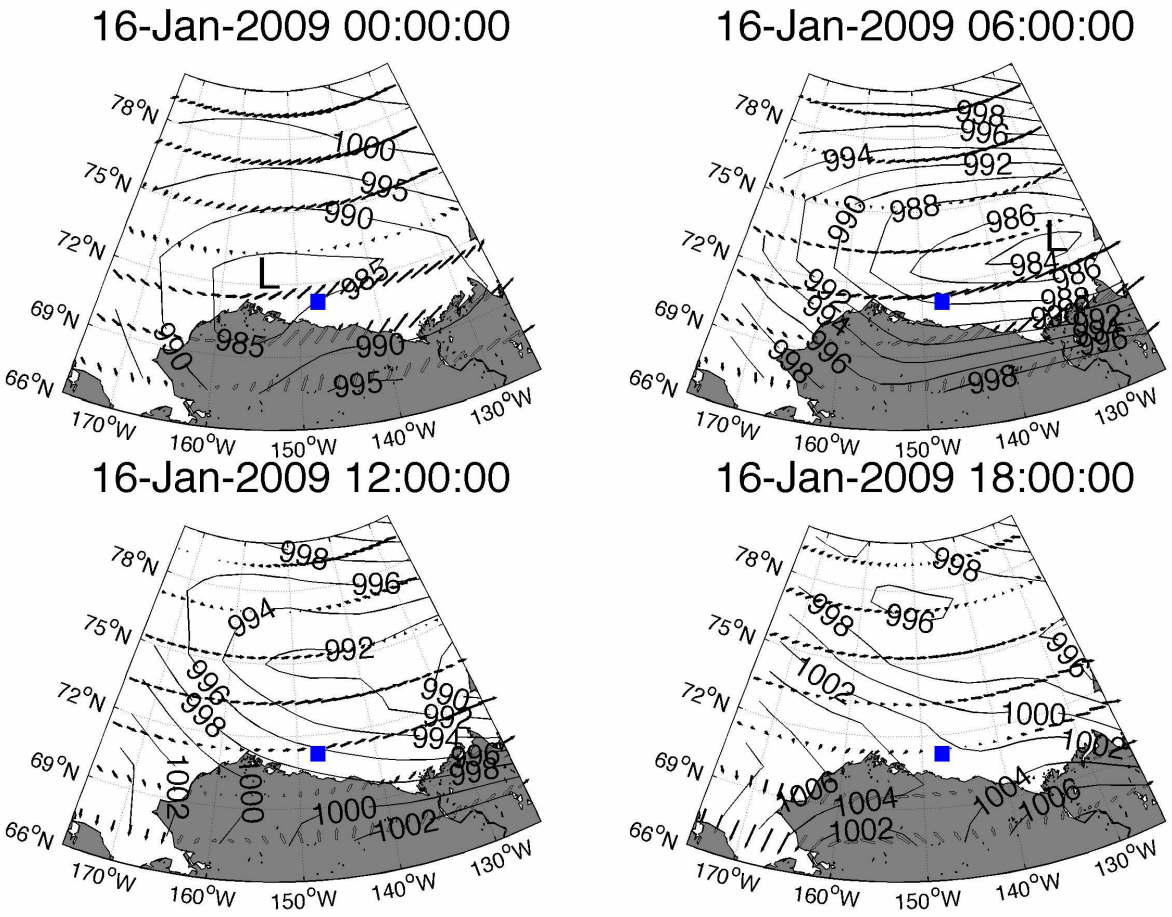

Figure 24: Low near-inertial power sea level pressure and wind map event 6. The ICORTAS mooring array location is indicated by the blue square.

3.8 April event 7

From 1200 April 26th to 0000 on April 27th, Barrow winds increased from 4 m s^{-1} to 10 m s^{-1} (Figure 25d). A large low pressure system moved slowly from Bering Strait directly north during this time, causing the winds to strengthen during this period (Figure 26) and slowly rotate from the south-southeast to the southwest. All I moorings showed the same increase in clockwise near-inertial energy, and B3 showed 3 times higher near-inertial energy (Figure 25a). Divergence decreased as the event progressed. The B3 inertial currents reached 5 cm s^{-1} immediately after the winds increased velocity (Figure 25b). The winds then died down to 1 m s^{-1} midday on April 28th. The clockwise near-inertial energy takes several days to decay. The lack of large observed divergence over the I1-I3 moorings and the different response observed at B3 suggests that the system, although not as strong as the earlier events, was able to barely overcome ice mechanics to excite a separate response at B3 (Figure 25c). However, the ice over the I moorings moved as a coherent unit.

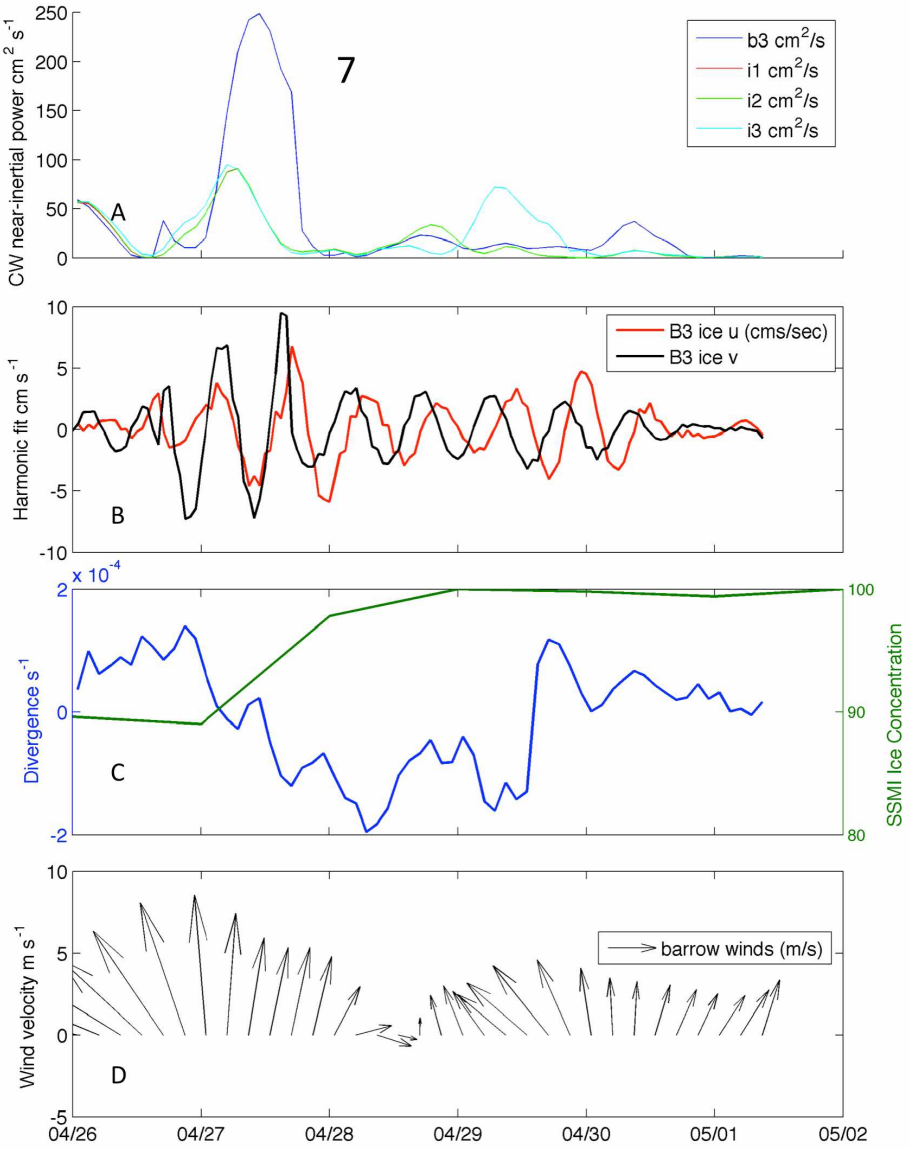

Figure 25: Low near-inertial power synthesis event 7. Storm event 7 composite of near-inertial ice energy (panel A), ice velocity harmonic fits (panel B), ice divergence (panel C), and winds (panel D) during low levels of near inertial energy observed in April 2009.

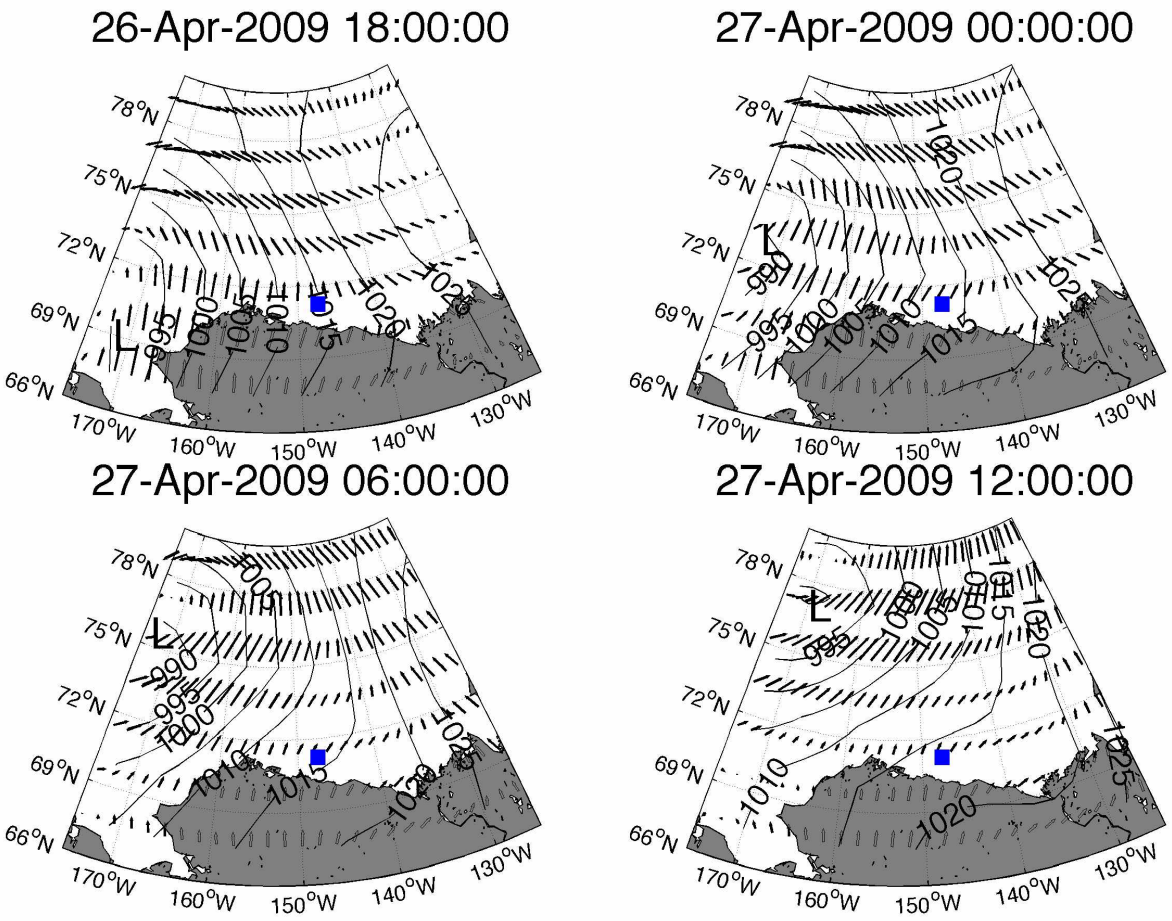

Figure 26: Low near-inertial power sea level pressure and wind map event 7. The ICORTAS mooring array location is indicated by the blue square.

4.0 Discussion

4.1 System time and space scales

The ratio of a storm's diameter (D_s, a length scale) to its translation speed (U_S, a velocity scale) defines the storm time scale, i.e., $T_S = D_S/U_S$. Note that U_S is not a measure of storm intensity. Lammert et al. [2009] showed that a passing low (or high) can resonantly force inertial ice oscillations if the diameter divided by the velocity of the storm was roughly equal to ¾ of the inertial period ($T_s \sim 0.75 T_{local}$).

For the ICORTAS region and time period, I found an enhanced near-inertial response for storm timescales between ¾ T_I and 1 ¼ T_I (Figure 27). For example, event 1 starting on December 11th had T_S (D/U)=15.4 h (diameter: 573 km, speed over ground: 37 m s^{-1}). Although a rise in near-inertial sea ice energy was observed, it was less than during later events that had a lower T_S value. The largest rise in sea ice near-inertial energy during December was observed 5 days later during event 2. The diameter of the storm was 615 km with a speed over ground of 60 m s^{-1}, giving the system a T_S=10.1 h, much closer to the inertial period. In February, event 3 starting in the morning of February 18th had a width of 706 km and a speed over ground of 75 m s^{-1}, giving the system a T_S=9.5 h. This acted to precondition the ice so that subsequent events had a greater impact upon the near-inertial energy in the ice than if there would have been no preconditioning. Eight days later event 4 occurred. This event stands out because it was a high pressure system that passed with the array on its left side. It had a width of 650 km and a speed over ground velocity of 63 m s^{-1} where T_S=10.2 h. This disturbance may have acted to precondition the ice for a large near-inertial response event 5, and at 0600 on March 7th another high impacted the array. The high moved quickly towards the array and caused a large increase in near-inertial ice oscillation energy. This event fed upon the preconditioned ice pack and caused a very large near-inertial response where T_S=15.3 h (diameter: 573 km, speed over ground: 37 m s^{-1}). The ice concentration decreased slightly and then increased to pre-event levels, after which the inertial oscillations were no longer observed probably due to refreezing. Thus, each event leaves behind an area of either open water or thinner ice.

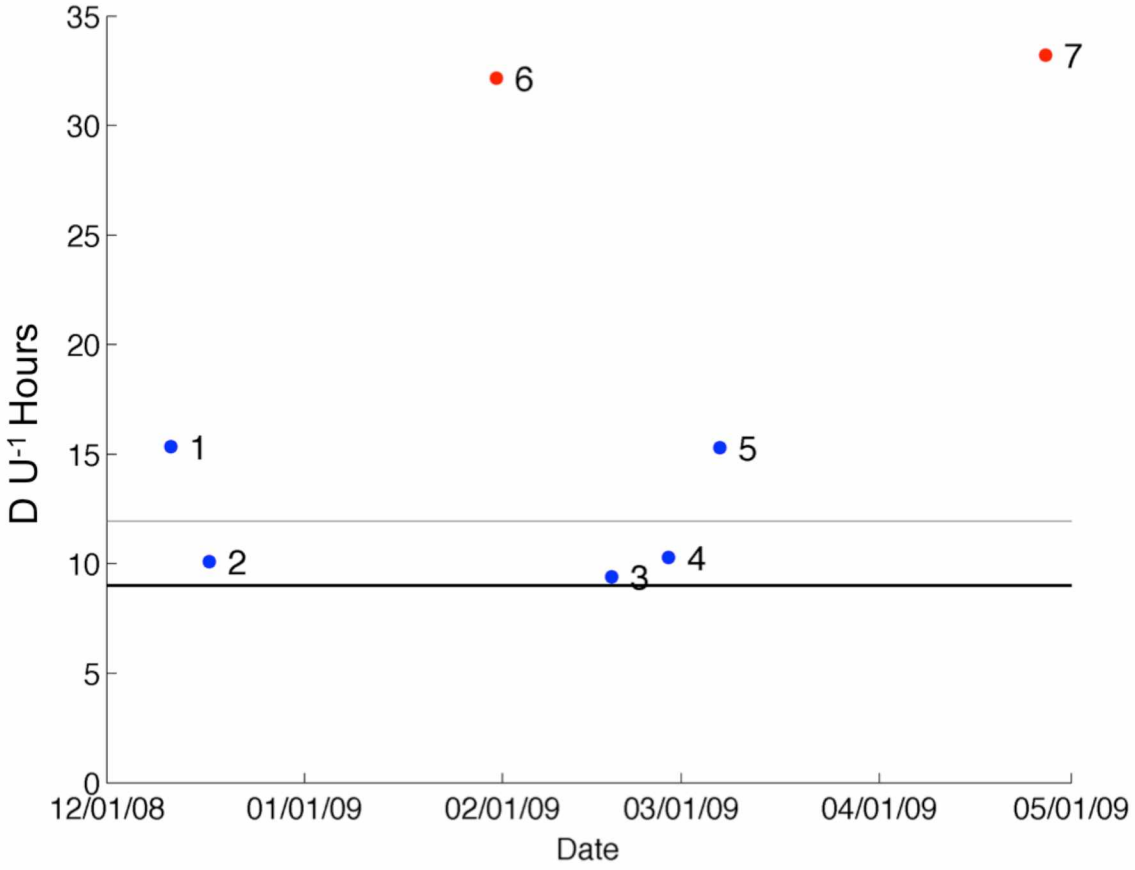

Figure 27: Storm timescale timeseries. $T_s = D\ U^{-1}$ during the 2008-2009 ICORTAS deployment. The black line indicates ¾ and one inertial period (9.6 – 12.6 h). Red dots are pressure systems that did not excite a significant near-inertial response. Blue dots are systems that excited a large near-inertial response. Individual events are labeled. The thin gray line corresponds to the local inertial period.

To contrast, events that excited little or no near-inertial response showed characteristics that included a large storm diameter, slow ground track speed, or some combination thereof. The first low response event 6 on January 31st had a width of 715 km and a ground track speed of 22 m $s^{-1}$with T_S=32.1 h. This speed over ground was approximately 3 times slower than the previously fast moving systems; however, the width of the system was about the same as those that excited a near-inertial response. The second low response near-inertial event 7 on April 27th was more complicated than the first, since the I moorings showed a small response but the B3 mooring did not. The system width was 1670 km and the speed over ground was 50 m s^{-1} with T_S=33 h. This system was almost 2.5 times larger in diameter than event 6, but moved at the same speed as systems that excited a near-inertial response.

Maximum near-inertial velocity and maximum wind speed of these systems were possibly correlated as shown in Figure 28. If sea ice were able to move freely, one would expect as wind velocity increases, sea ice velocity would also increase in a linear fashion. However, this relationship was not clearly evident with two events (3 and 5) that had higher maximum near-inertial velocities but lower wind velocities than events 7 and 6, respectively. It is hypothesized that sea ice mechanics were modifying this relation; however, events 1, 2 and 4 did show an increase in near-inertial energy associated with increasing winds. In addition Martini et al. [2014] showed near-inertial internal wave generation concurrently during periods of observed high ice near-inertial energy, suggesting a link between the two. Inertial currents observed during the ice-free season driven by local storms can exceed 20 cm s^{-1} in the northern Chukchi Sea, and near-inertial ice motion observed in the ICORTAS experiment reached similar values with the maximum exceeding 20 cm s^{-1}.

Figure 29 shows the relation between mean divergence during the event and T_s (D/U) ratio. The two high pressure systems events (4 and 5) had positive divergence about 2 times smaller than the smallest low pressure convergence values. The three low pressure events all had negative divergence values or convergence (1, 2 and 3). Sea ice convergence in response to low pressure system and divergence in response to a high pressure system were expected results [*Hibler III. and Bryan*, 1987]. All five of these events had low T_s. Interestingly, the two events with high T_s values (6 and 7) showed little or no divergence or convergence. This means that at lower T_s values the ice pack diverges or converges. At higher T_s values the ice pack moves together as a coherent unit with little to no divergence/convergence.

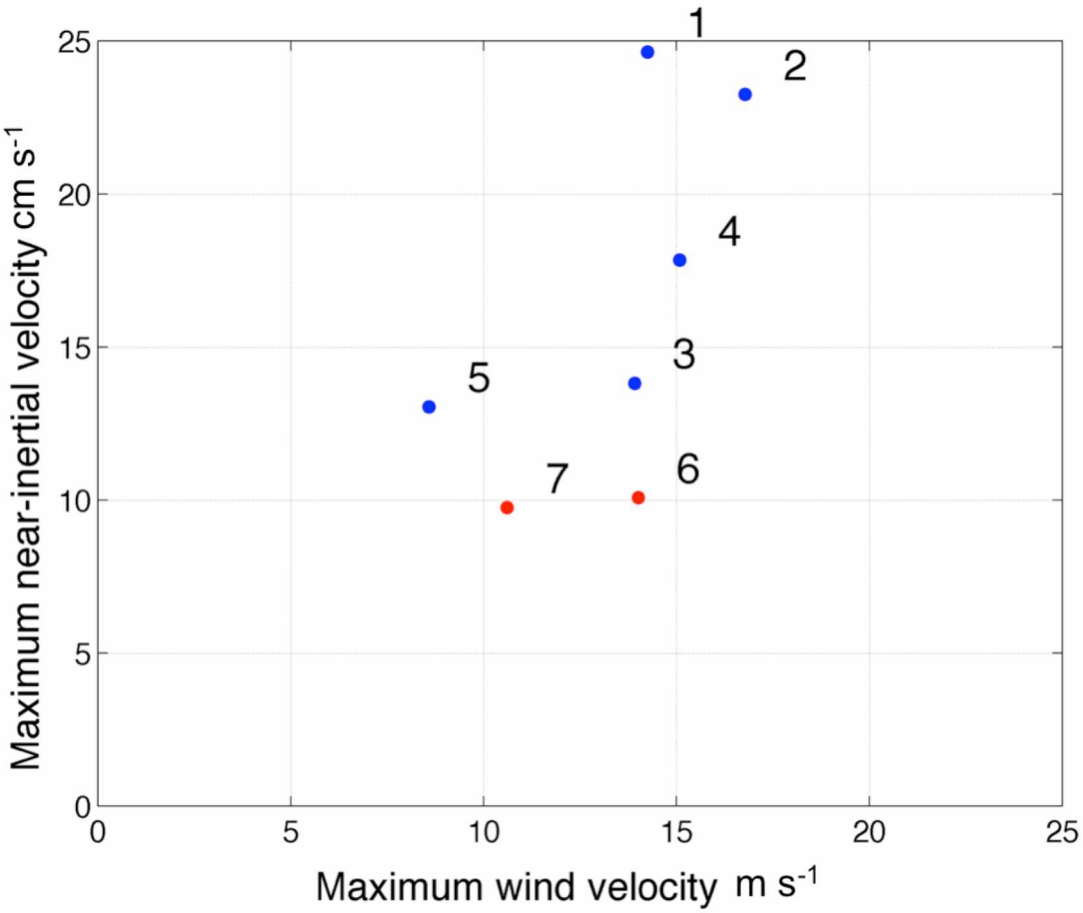

Figure 28: Maximum near-inertial velocity versus maximum wind velocity. Red dots are pressure systems that did not excite or excited a tiny near-inertial response. Blue dots are systems that excited a large near-inertial response.

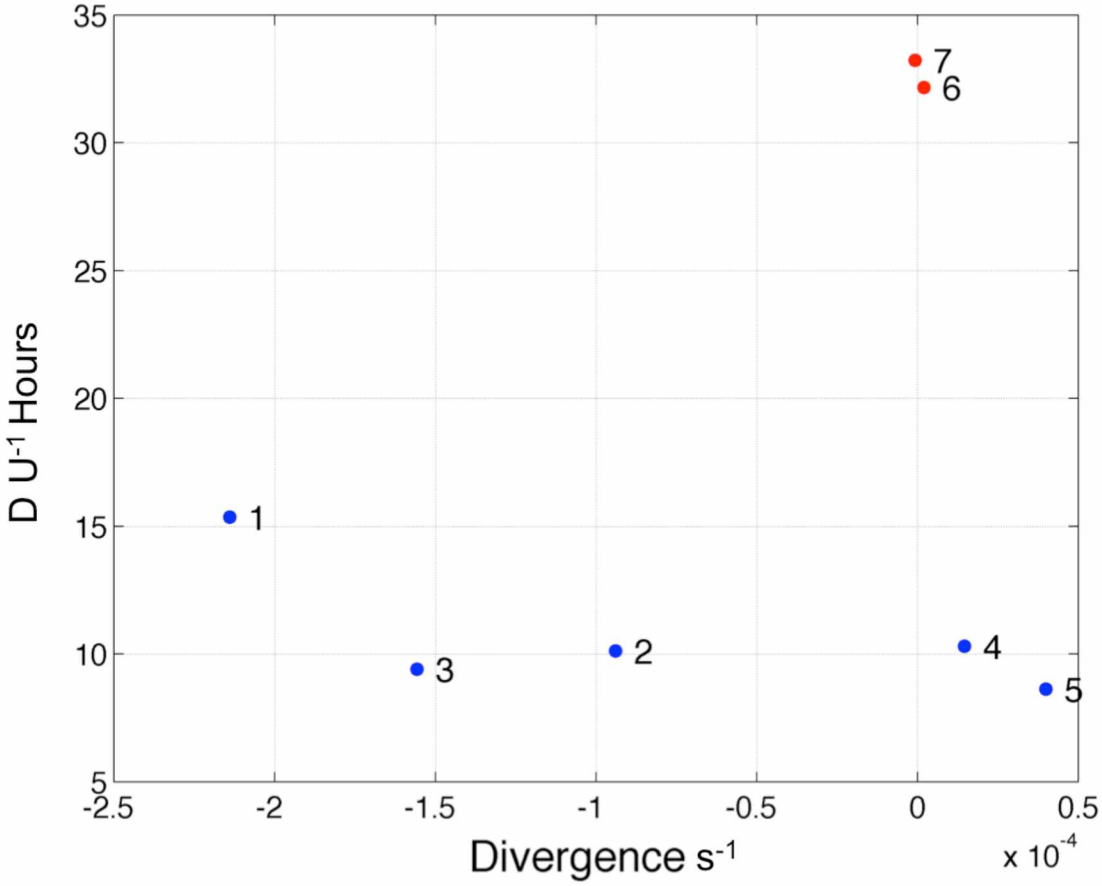

Figure 29: D U^{-1} (i.e., T_S) versus divergence. Red dots are pressure systems that did not excite or excited a tiny near-inertial response. Blue dots are systems that excited a large near-inertial response.

4.2 Comparison with other studies

Several sea ice properties in the Arctic have changed considerably over the last decade. Sea ice mean speed across the Arctic has increased at a rate of 9% per decade starting in 1979 [*Rampal et al.*, 2009]. Over the same period, deformation has increased at a rate of 50% per decade [*Rampal et al.*, 2009]. This increased deformation and motion coupled with decreasing sea ice extent in the Arctic has led to an increasing albedo feedback loop where more open water absorbs more thermal energy, further melting ice and exposing more open water [*Zhang et al.*, 2000]. The near-inertial response of sea ice has not received a great deal of attention, exceptions are studies by Hunkins [1967] who observed near-inertial ice motion from a manned ice island station. Colony and Thorndike [1980] and Thorndike and Colony [1982] separated out the near-inertial signal from the lower frequency ice drifter motion in response to wind forcings. More recent studies include Heil and Hibler [2002], who found that by incorporating sea ice near-inertial motion, modeling results were able to accurately describe buoy ice drift data. Gimbert et al. [2012] calculated a sea ice near-inertial motion index using the International Arctic Buoy Program (IABP) dataset. They found a strong seasonal signal in ice near-inertial motion that largely follows extent, concentration, thickness, velocities and deformation rates. Summer sea ice near-inertial motion was greater than winter sea ice near-inertial motion simply because of the larger ice free area. The near-inertial ice motion spatial patterns were also in agreement with thickness and concentration patterns, where areas of thicker ice and high concentrations (e.g., northern Greenland) have low near-inertial energy. In the Gimbert et al. [2012] study, near-inertial energy adjacent to the ICORTAS array was near zero in the winter. I suggest that this was a sampling artifact due to the kind of ice IABP buoys are deployed in, which require ice thick enough to support instrumentation. Since thinner ice is associated with higher speeds [*Rampal et al.*, 2011], IABP data represent undersampled sea ice types with respect to near-inertial oscillations. Furthermore, the ICORTAS array was deployed in an interface zone between the Beaufort gyre and shorefast ice; thus, any buoys deployed in the gyre or pack ice are unlikely to traverse the mooring array area. Also, some IABP buoys have been deployed with sensor strings longer than the water depth at which the array was moored; therefore, the results in Gimbert et al. [2012] represent undersampling in the ICORTAS region. Gimbert et al. [2012] used change point analysis to identify two statistically different regimes for the time periods 1979-2001 versus 2002-2008. During both periods the winter and summer near-inertial energy

increased in the 2002-2008 period linked to the loss of sea ice. As sea ice loss continues, sea ice near-inertial oscillations are expected to increase. In summary, the data from the ICORTAS array demonstrated that near-inertial oscillations occur more often in this area of the Beaufort than previously thought when compared to Gimbert et al. [2012]. A further increase in sea ice near-inertial oscillations will lead to an increase in energy transferred from the atmosphere through the sea ice into the ocean below in this region [*Martini et al.*, 2014].

5.0 Summary and Conclusions

Acoustically derived sea ice concentrations from a mooring array correlated well with passive microwave satellite data. Sea ice inertial motions in response to wind were identified and distinguished from other sea ice motion. Two episodes of long lasting near-inertial power were observed, comprised of several high frequency wind shift events.

5.1 What do we learn from the ADCP ice concentration estimates that do not have the spatial and temporal biases of SSMI?

The mooring derived concentration time series was more sensitive than SSMI data to sea ice formation as well as melting and small-scale features that traverse the array. Overall, this method provided a reasonable comparison to SSMI data, especially with the known [*Comiso*, 1986] satellite issues encountered during freeze up and melt.

The 91.7 km^2 footprint of the array detects features that the 625 km^2 SSMI footprint may not completely observe. For example, as discussed previously in section 3.1, for the observed lead that was 60 km long, drifting at 30 cm s^{-1} and was oriented in the direction of the array, mooring derived sea ice concentrations would be zero for 2 days while SSMI concentrations would be 70-80%. Observed features during event 1 such as the decrease in nearshore ice concentration southeast of the mooring array were easily visible in SSMI but were not observed in the array even though this region abuts the array. Features with scales that were less than the distance between individual moorings can contribute to vastly different ice concentrations measurements across the array. The combination of the small-scale resolution of the array and the larger spatial context provided by SSMI provides a unique view of spatial and temporal variability of sea ice concentration.

5.2 Can we identify sea ice inertial motions in response to the wind?

Data from the ICORTAS array showed clockwise near-inertial energy at the local inertial frequency. Examination of these events in conjunction with analysis of wind data from Barrow

and NCEP showed that the events occurred in response to atmospheric systems with particular timescales. To be most effective, the pressure systems responsible for the wind shifts must have the appropriate time scale resulting from the ratio of storm diameter to speed over ground, forcing the ice impulsively over a time scale of 9-15 h. Martini et al. [2014] linked the occurrence of high near-inertial internal wave activity events to associated atmospheric events, specifically to fast moving, small-diameter storms. This study found that, while forcing events were associated with low-pressure system, near-inertial sea ice energy can also arise from translating high pressure systems. Large increases in sea-ice near inertial energy were observed during decreases in sea ice concentration in this study, thus suggesting that space must be available for the ice pack to oscillate in a near-inertial fashion. Furthermore, sea ice near-inertial response was very event specific. The two events described for February appeared to build upon earlier preconditioning events, which allowed the ice to respond more freely to smaller inputs. Large sea ice velocities during these events also suggest that wind was the dominant forcing factor, since all other forcings could not account for such a large observed velocity; however, this effect was modified by the ice pack strength.

5.3 How often do wind forced sea ice near-inertial oscillations occur and what system characteristics cause these oscillations in the Beaufort?

Pressure systems that moved quickly over the array and had a small diameter (diameter/velocity was close to ¾ of the local inertial period) stimulated a larger near-inertial response in the sea ice compared with systems that were large and slow moving, which excited a smaller near-inertial response. Pressure systems that were both small and fast moving may be powerful enough to overcome ice mechanics to the point where sea ice can move inertially. Ice mechanical characteristics that need to be considered in this context were, for example, ice strength, deformation, friction, and thickness distribution [*Hibler III. and Bryan*, 1987]. Interestingly, preconditioning events can cause divergence that allows later events to move sea ice inertially with less effort. Conclusively, every storm system that crosses the Arctic will excite a different response depending on its geographical distribution, ice strength, previous systems in the same area, and speed over ground.

5.4 Implications and future work

Winter energy transfer events may be more common than previously thought throughout the Arctic Ocean, as evidenced by the two observed mid-winter events. Observations of high

near-inertial energy in winter sea ice coinciding with increased oceanic activity suggest that this may happen in other parts of the ice-covered Arctic Ocean. However, the characteristics vary from storm system to system, and specific conditions must be met for near-inertial sea ice oscillations to occur. Further reanalysis work quantifying the frequencies and geographical distribution of pressure systems that satisfy T_S requirements for sea ice near-inertial oscillations may help guide future studies. However, high temporal resolution measurements combined with the geographical resolution needed for divergence limits the feasibility of any future studies to specific areas of the Arctic basin, thus making it difficult to confirm how these systems stimulate near-inertial sea ice response on a basin-wide scale.

Rainville and Woodgate [2009] showed low inertial energy in both the ocean and sea ice during the Arctic winter. The numerous inertial events during winter with high sea ice concentration identified in this study provide a counterexample and it is thought the proximity of the Chukchi polynya [*Tamura and Ohshima*, 2011] and the relatively low sea ice concentrations near the polynya could contribute to this phenomenon. It seems likely that these processes could be observed in proximity to other coastal polynyas and marginal ice zones, which are prevalent throughout the Arctic coastal regions [*Tamura and Ohshima*, 2011]. The present study identified numerous examples of the effectiveness of small diameter, fast moving Arctic cyclones in exciting inertial energy in the ice-pack. If future climate conditions result in an increase in transient leads along with a greater distribution of polynyas, this could increase kinetic energy transfer into the upper ocean and ultimately increase heat transfer to the atmosphere through enhanced upper ocean mixing.

6.0 References

Aagaard, K., and P. Greisman (1975), Toward new mass and heat budgets for the Arctic Ocean, *Journal of Geophysical Research*, *80*, 3821–3827.

Aagaard, K., L. K. Coachman, and E. C. Carmack (1981), On the halocline of the Arctic Ocean, *Deep-Sea Research 28A*, 529–545.

Armstrong, R. L., and M. J. Brodzik (2002), Hemispheric-scale comparison and evaluation of passive microwave snow algorithms., *Annals of Glaciology*, *34*, 38-44.

Asplin, M. G., J. V. Lukovich, and D. G. Barber (2009), Atmospheric forcing of the Beaufort Sea ice gyre: Surface pressure climatology and sea ice motion, *Journal of Geophysical Research*, *114*, 1-13.

Berry, D. I., and E. C. Kent (2011), Air-Sea fluxes from ICOADS: the construction of a new gridded dataset with uncertainty estimates, *International Journal of Climatology*, *31*, 987–1001.

Carmack, E. C. (2007), The alpha/beta ocean distinction: A perspective on freshwater fluxes, convection, nutrients and productivity in high-latitude seas, *Deep-Sea Research II 54*, 2578–2598.

Cassano, E. N., J. J. Cassano, M. E. Higgins, and M. C. Serreze (2013), Atmospheric impacts of an Arctic sea ice minimum as seen in the Community Atmosphere Model, *International Journal Of Climatology*, *34*, 766-779.

Colony, R., and A. S. Thorndike (1980), The Horizontal Coherency of the Motion of Summer Arctic Sea Ice, *Journal of Physical Oceanography*, *10*, 1281-1289.

Comiso, J. C. (1986), Characteristics of Arctic winter sea ice from satellite multispectral microwave observations. , *Journal of Geophysical Research 91*, 975-994.

Emery, W. J., and R. E. Thomson (2001), *Data Analysis Methods in Physical Oceanography*, 2 ed., Boulder, CO.

Fetterer, F., and J. Hawkins (2003), AVHRR Leads-ARI Polar Gridded Brightness Temperatures, edited by NOAA, NSIDC, Boulder, Colorado USA.

Fiedler, E. K., T. A. Lachlan-Cope, I. A. Renfrew, and J. C. King (2010), Convective heat transfer over thin ice covered coastal polynyas, *Journal of Geophysical Research*, *115*, 1-19.

Gill, A. E. (1984), On the Behavior of Internal Waves in the Wakes of Storms, *Journal of Physical Oceanography*, *14*, 1129-1151.

Gimbert, F., D. Marsan, J. Weiss, N. Jourdain, and B. Barnier (2012), Sea ice inertial oscillations in the Arctic Basin, *The Cryosphere*, *6*, 1188-1201.

Halle, C., and R. Pinkel (2003), Internal Wave variability in the Beaufort Sea during the winter of 1993/1994, *Journal of Geophysical Research*, *108*, 1-23.

Heil, P., and W. D. Hibler III. (2002), Modeling the High-Frequency Component of Arctic Sea Ice Drift and Deformation, *Journal of Physical Oceanography*, *32*, 3039-3057.

Heil, P., J. Hutchings, A. Worby, M. Johansson, J. Launiainen, C. Haas, and W. D. Hibler III. (2008), Tidal forcing on sea-ice drift and deformation in the western Weddell Sea in early austral summer, 2004, *Deep-Sea Research II*, *55*, 943-962.

Hibler III., W. D. (2004), Modelling the dynamic response of sea ice, in *Mass Balance of the Cryosphere*, edited by J. L. Bamber and A. J. Payne, pp. 227-334, Cambridge University Press.

Hibler III., W. D., and K. Bryan (1987), A diagnostic ice-ocean model, *Journal of Physical Oceanography*, *17*, 987-1015.

Hibler III., W. D., I. Udin, and A. Ullerstig (1983), On forecasting mesoscale ice dynamics and buildup., *Annals of Glaciology*, *4*, 110-115.

Hibler III., W. D., W. F. Weeks, A. Kovacs, and S. F. Akcley (1974), Differential sea ice drift I: spatial and temporal variations in sea ice deformation, *Journal of Glaciology*, *31*, 437- 455.

Hibler III., W. D., P. R. Heil, A. Y. Proshutinsky, H. L. Simmons, and J. Lovick (2006), Modeling M2 Tidal Variability in Arctic Sea-Ice Drift and Deformation, *Annals of Glaciology*, *44*, 418-428.

Hunkins, K. (1967), Inertial oscillations of Fletcher's Ice Island (T-3), *Journal of Geophysical Research*, *72*, 1165-1174.

Hutchings, J. K., P. R. Heil, and W. D. Hibler III. (2005), On Modelling Linear Kinematic Features in Sea Ice, *Monthly Weather Review*, *133*, 3481-3497.

Jacobs, S. S., and J. C. Comiso (1989), Sea ice and oceanic processes on the Ross Sea continental shelf, *Journal of Geophysical Research*, *94*, 18195–18211.

Kanamitsu, M., W. Ebisuzaki, J. Woollen, S.-K. Yang, J. J. Hnilo, M. Fiorino, and G. L. Potter (2002), NCEP-DOE AMIP-II Reanalysis (R-2), *Bulletin of the American Meteorological Society*, 1631-1643.

Khandekar, M. R. (1980), Inertial oscillations in floe motion over the Beaufort - observations and analysis, *Atmosphere-Ocean*, *18*, 1-14.

Koç, N., N. B., R. Armstrong, R. W. Correl, D. D. Jensen, K. R. Leslie, A. Rivera, Y. Tandong, and J. G. Winther (2009), Melting snow and ice: a call for action. *Rep.*, Centre for Ice, Climate and Ecosystems, Norwegian Polar Institute.

Kowalik, Z., and A. Y. Proshutinsky (1993), Diurnal Tides in the Arctic Ocean *Journal of Geophysical Research*, *98*, 449-468.

Kurtz, N. T., T. Markus, S. L. Farrell, D. L. Worthen, and L. N. Boisvert (2011), Observations of recent Arctic sea ice volume loss and its impact on ocean-atmosphere energy exchange and ice production, *Journal of Geophysical Research*, *116*, 1-19.

Kwok, R. (2006), Contrasts in sea ice deformation and production in the Arctic seasonal and perennial ice zones, *Journal of Geophysical Research: Oceans (1978–2012)*, *111*, 1-14.

Kwok, R., G. F. Cunningham, and W. D. Hibler III. (2003), Sub-daily sea ice motion and deformation from RADARSAT observations, *Geophysical Research Letters*, *30*, 2218-2212.

Lammert, A., B. Brummer, and L. Kaleschke (2009), Observation of cyclone-induced inertial sea ice oscillation in Fram Strait, *Geophysical Research Letters*, *36*, 1-5.

Lepparanta, M., and W. D. Hibler III. (1985), The role of plastic ice interaction in marginal ice zone dynamics, *Journal of Geophysical Research*, *90*, 11899-11909.

Markus, T., and D. J. Cavalierie (2000), An Enhancement of the NASA Team Sea Ice Algorithm, *IEEE transactions on geoscience and remote sensing 38*, 1387-1399.

Martini, K., H. L. Simmons, C. A. Stoudt, and J. Hutchings (2014), Near-inertial internal waves and sea ice in the Beaufort Sea, *Geophysical Research Letters*, *44*, 2212–2234.

Nolin, A. W., R. Armstrong, and J. Maslanik (1998), Near-Real-Time SSM/I-SSMIS EASE-Grid Daily Global Ice Concentration and Snow Extent. Version 4, edited by NSIDC, Boulder, Colorado, USA.

Padman, L., and S. Erofeeva (2004), A barotropic inverse tidal model for the Arctic Ocean, *Geophysical Research Letters*, *31*, 1-8.

Parkinson, C. L., and J. C. Comiso (2013), On the 2012 record low Arctic sea ice cover: Combined impact of preconditioning and an August storm, *Geophysical Research Letters*, *40*, 1356-1361.

Perovich, D. K., B. Light, H. Eicken, K. F. Jones, K. Runciman, and S. V. Nghiem (2007), Increasing solar heating of the Arctic Ocean and adjacent seas, 1979–2005: Attribution and role in the ice-albedo feedback, *Geophysical Research Letters*, *34*, 1-5.

Pickart, R. S., G. W. K. Moore, D. J. Torres, P. S. Fratantoni, R. A. Goldsmith, and J. Yang (2009), Upwelling on the continental slope of the Alaskan Beaufort Sea: Storms, ice, and oceanographic response, *Journal of Geophysical Research*, *114*, 1-17.

Pollard, R. T., and R. C. Millard, Jr. (1970), Comparison between obseved and simulated wind-generated inertial osciallations *Deep-Sea Research*, *17*, 813-816.

Price, J. F., R. A. Weller, and R. Pinkel (1986), Diurnal cycling: Observations and models of the upper ocean response to diurnal heating, cooling, and wind mixing, *Journal of Geophysical Research*, *91*, 8411–8427.

Proshutinsky, A. Y., and M. A. Johnson (1997), Two circulation regimes of the wind-driven Arctic Ocean, *Journal of Geophysical Research*, *102*, 12493-12514.

Proshutinsky, A. Y., R. H. Bourke, and F. A. McLaughlin (2002), The role of the Beaufort Gyre in Arctic climate variability: Seasonal to decadal climate scales, *Geophysical Research Letters*, *29*, 2100-2115.

Rainville, L., and R. R. Woodgate (2009), Observations of internal wave egneration in the seasonally ice-free Arctic, *Geophysical Research Letters*, *36*, 1-5.

Rampal, P., J. Weiss, and D. Marsan (2009), Positive trend in the mean speed and deformation rate of Arctic sea ice, 1979–2007, *Journal of Geophysical Research*, *114*, 1-14.

Rampal, P., J. Weiss, C. Dubois, and J. Campin (2011), IPCC climate models do not capture Arctic sea ice drift acceleration: Consequences in terms of projected sea ice thinning and decline, *Journal of Geophysical Research*, *116*, 1-17.

Serreze, M. C., and A. P. Barret (2007), The Summer Cyclone Maximum over the Central Arctic Ocean, *Journal of Climate*, *21*, 1048-1065.

Stranne, C., and G. Bjork (2012), On the Arctic Ocean ice thickness response to changes in the external forcing, *Climate Dynamics*, *39*, 3007-3018.

Stroeve, J. C., M. C. Serreze, M. M. Holland, J. E. Kay, J. Malanik, and A. P. Barret (2012), The Arctic's rapidly shrinking sea ice cover: a research synthesis, *Climatic Change*, *110*, 1005-1017.

Tamura, T., and K. I. Ohshima (2011), Mapping of sea ice production in the Arctic coastal polynyas, *Journal of Geophysical Research*, *116*, 1-20.

Teledyne (2006), Accoustic Doppler Current Profiler Principles of Operation A Practical Primer*Rep.*, Poway.

Thorndike, A. S., and R. Colony (1982), Sea Ice Motion in Response to Geostrophic Winds, *Journal of Geophysical Research*, *87*, 5845-5822.

Van Meurs, P. (1998), Interactions between Near-Inertial Mixed Layer Currents and the Mesoscale:
The Importance of Spatial Variabilities in the Vorticity Field, *Journal of Physical Oceanography*, *25*, 1363-1388.

Visbeck, M., and J. Fischer (1995), Sea Surface Conditions Remotely Sensed by Upward-Looking ADCPs *American Meterological Society* 141-149.

Willmes, S., M. Nicolaus, and C. Haas (2013), The microwave emissivity variability of snow covered first-year sea ice from late winter to early summer: a model study, *The Cryosphere*, *7*, 891-904.

Zhang, J., D. Rothrock, and M. Steele (2000), Recent Changes in Arctic Sea Ice: The Interplay between Ice Dynamics and Thermodynamics, *Journal of Climate*, *13*, 3099–3114.